A New Approach to Wide Bandwidth Energy Harvesting for Piezoelectric Cantilever Based Harvesters

John Andrew Turner

Dissertation submitted to the faculty of the
Virginia Polytechnic Institute and State University
in partial fulfillment of the requirements for the degree of

Masters of Science
in
Electrical Engineering

Dong S. Ha, Chairman
Kathleen Meehan
K. J. Koh

January 28th, 2013
Blacksburg, VA

Keywords: Energy Harvesting, Piezoelectric Cantilevers, Power Management, DC-DC Converter, Impedance Matching

Abstract

This thesis proposes a control system to widen the bandwidth of piezoelectric transducers (PZTs) for vibration energy harvesting while extracting maximum power. A straightforward complex conjugate match achieves maximum power transfer only at a single frequency while requiring an impractically large inductance. The proposed system intends to address these problems. It incorporates a bi-directional DC/DC converter with feed-forward control to achieve a complex conjugate match over a wide range of frequencies. Analysis of the proposed system and simulation results are presented to verify validity of the proposed method.

Acknowledgements

I would like to express the sincerest of thanks to the people who have helped and supported me, academically and otherwise during my time at Virginia Tech.

First I would like to thank Dr. Ha, who not only provided me with his technical expertise and guidance, necessary for me to do this research, but who also plans and organizes many social events, reminding us that there is life outside of work. I would like to give him my sincerest of thanks, for providing an environment where I could not only do this research, but enjoy it.

I am very grateful for Dr. Paolo Mattavelli, who was not only part of the original research that inspired my thesis, but took time to talk with me about my work, and made suggestions that would influence and shape the direction my research went.

I am grateful to Dr. Daniel Inman, and Dr. Priya with the Center for Intelligent Material Systems and Structures (CIMMS) for providing me with opportunities for interdisciplinary energy harvesting research, and the opportunity to design converters for their new energy harvesting mechanical systems. I would also like to thank Justin Farmer and Anthony Marin of CIMSS, for their help with this work.

I would also like to express my appreciation to all the members of Dr. Ha's lab for their support and friendship – Travis Cochran, Justin Cartwright, Na Kong, Jin Yun, Jihoon Yun, Maruf Ahmed, and Jebreel Salem.

Finally I would like to thank my girlfriend Marian, and my parents, John and Belinda Turner, who have all provided support when I've needed it.

Table Of Contents

List Of Figures

List Of Tables

1: Introduction

1.1 Energy Harvesting in the Modern World

As modern advances continue to miniaturize wireless communications, as well as reduce power consumption, new and exciting applications become possible. Wireless Sensor Nodes (WSNs) consisting of many small sensors and radios are becoming a common area of interest for researchers, due to the interesting challenges associated with creating networks of WSNs, which have been used in a variety of applications [1].

The powering of WSNs is a particularly interesting and difficult challenge for modern electronics to tackle. Most WSNs are not placed near permanent power sources, and must either scavenge energy from the environment, or operate using only stored energy. Use of batteries is the easiest solution but in many cases batteries are not the optimal solution. While research has gone into various methods of reducing power consumption all batteries will eventually run out of energy, requiring their replacement [2]. Replacing of batteries is labor intensive and expensive, requiring the node to be in a location that can be accessed again, and generates unnecessary waste. From a size standpoint, batteries are frequently one of the largest components on the board, increasing the overall size and weight of the final package.

A viable and popular alternative to batteries, in many applications is energy harvesting, which has received a great deal of research in recent history, both in energy sources and wireless networking techniques [1, 3-5]. Energy harvesting techniques scavenge energy from the environment that would otherwise be wasted, and uses it to power the circuits or electronics. Using energy harvesting techniques, devices such as WSNs may theoretically be perpetually powered, never needing to have batteries replaced.

The most popular sources for harvesting energy are solar power, thermal power, vibration energy, and RF energy. Of the four, solar power has the highest energy density by far, but is not always a viable option for energy harvesting, due to lack of sun in certain locations and times of day. This research focuses on vibration energy harvesting, which is abundant in many environments stable and predictable in practical applications [6].

1.2 Overview of Vibration Energy Harvesting

There are three main types of vibration energy harvesting: piezoelectric transducer (PZT) based energy harvesting, electromagnetic energy harvesting, and electrostatic energy harvesting. All three types of vibration energy harvesting convert mechanical energy into electrical energy, through various transduction methods, which will be discussed here.

EM harvesters are a popular way to harvest vibration energy. EM harvesters generate electricity by moving a magnet/magnetic field over a coiled wire. As the magnetic field through the coiled wire changes, the wire generates an electrical current which may be harvested. Because the magnetic field in the harvester will both increase and decrease, the current generated by the wire is AC, requiring a back-end circuit to both rectify and regulate the power from the EM coil.

EM harvesters can come in many shapes and sizes, with the only real limitation being a configuration where the magnetic field through a coil changes. Many EM vibration harvesters rely on resonant structures, which can be modeled as mass-spring damper systems. These are advantageous because of high power density, but are only capable of harvesting energy from a specific frequency. If there is not much energy available at the frequency of vibration, resonant harvesters are ineffective, as they harvest very little energy from frequencies other than

resonance [7]. Figure 1.1 shows a typical EM resonance harvester, based on a mass spring damper system. The magnet acts as the mass as well as a source of magnetic energy for the changing field. The magnet is placed on a spring, with a resonant frequency determined by the spring stiffness and magnet weight. As the magnet movies up and down, the field through the coil changes, and current is generated.

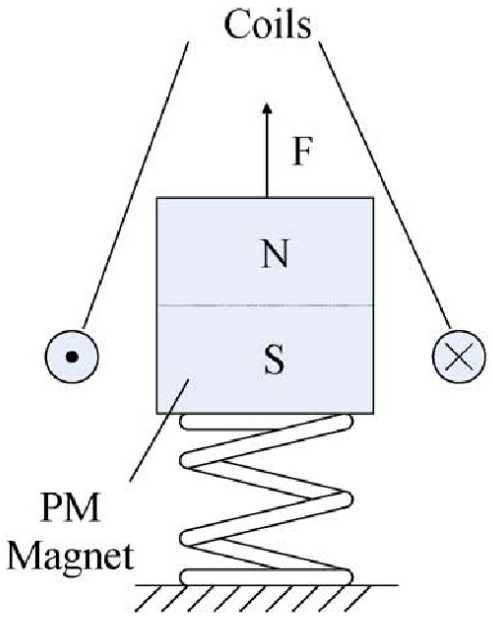

Figure 1.1 A mass-spring damper resonant EM harvester [7]

Electrostatic energy harvesting is a method of harvesting vibration energy from a variable capacitor or "varactor." This technique is typically used to harvest energy from simple parallel plate capacitors. Vibrations move the spacing of the capacitor plates, which in turn changes the capacitance of the capacitor, and the force exerted on the capacitor changes the energy stored. Due to the complication that no energy is harvested if the capacitor does not have voltage across it while the value changes electrostatic energy harvesting requires an investment of energy each

cycle. Electrostatic energy harvesting tends to be very low power, and is most suitable for very small and very low power systems [6].

Piezoelectric energy harvesting relies on piezoelectric transducers, which produce an electrical current when placed under mechanical strain. These devices can be used to turn mechanical energy into electrical energy. Like EM energy harvesting, there are many different methods of harvesting from PZT devices. Some methods rely directly on compression of PZT devices, while other configurations create resonant systems, targeting a specific frequency. PZT cantilevers are one of the most popular vibration energy harvesting techniques. PZT cantilevers consist of a beam with a mass at the tip of the beam, and piezoelectric material that is forced to bend with the beam. When excited at the resonant frequency, these devices have a high energy density.

Of the three discussed topologies, electrostatic energy harvesting is for the lowest power systems, and cannot yet provide enough power for most WSNs today. EM energy harvesters tend to be most effective in larger systems, but do not generate as much power as PZTs can in the 1-10 mW range. PZT cantilevers have very high energy densities when excited at the resonant frequency, and are good sources of power for WSNs. For these reasons, PZT cantilevers will be the harvesting source of focus for this paper and will be analyzed in depth in the Background section.

1.3 Proposed Approach and Contributions

This research will present a novel approach to regulating energy harvested from PZT cantilevers. There are many challenges associated with regulating energy harvested from PZT cantilevers. Firstly, the energy from PZT cantilevers is typically a high voltage AC signal. As

not many small-scale electronics can run off of AC power, this necessitates rectification, and DC-DC power regulation, or more complicated and less efficient AC-DC rectification.

Another challenge when harvesting from PZT cantilevers is impedance matching. PZT cantilevers have complex source impedances, and the output power can vary drastically based on the input impedance of the next stage. Effective converters must have well matched input impedance near resonance in order to extract maximum power.

The proposed converter uses a feed forward network to force the input impedance to that of the best match of the controller. A DC offset on the PZT output impedance allows for direct DC-DC conversion without the need of rectification, and a carefully defined input impedance matches the PZT at resonance, and widens the range of resonant frequencies. It will be shown that this method allows for superior power extraction when compared to other methods, at the expense of more complex control.

This research on power management for PZT cantilevers has the following contributions:

(i) The design analysis, and theoretical results for a novel power management circuit for PZT cantilevers which allows for wider bandwidth impedance matching of PZT cantilevers, while effectively regulating the power.

(ii) Simulation results which confirm the analysis, and show that this method can improve energy harvested from PZT cantilevers.

2: Background

This section details modeling of PZT cantilevers, both mechanical and electrical. Using these models, theoretical methods of maximum power transfer are examined, and existing approaches to extracting power from PZTs are discussed.

2.1 Electrical Model for Piezoelectric Cantilevers

Piezoelectric cantilevers are a popular method of energy harvesting from PZT devices due to the relatively high electromechanical coupling of PZT materials, and the high energy density of cantilever structures. For these reasons, PZT cantilevers will be the harvesting device of this thesis research.

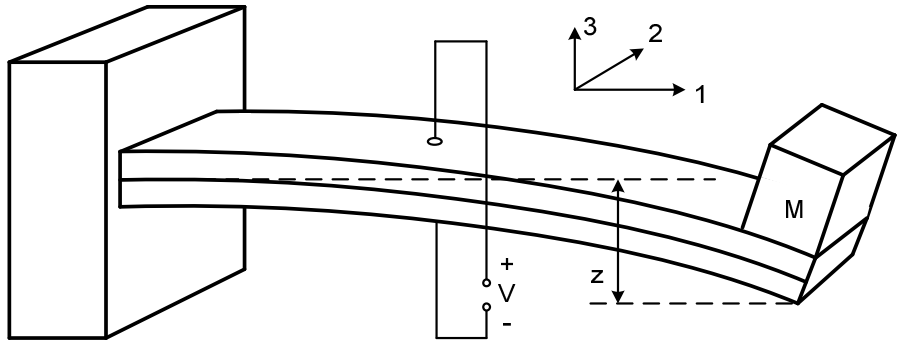

Figure 2.1 Typical dual layer PZT cantilever

Figure 2.1 shows a typical PZT cantilever, which consists of a long beam, fixed to a vibrating structure, and a tip mass. The beam has two layers of piezoelectric material, which generates a voltage when a mechanical strain is applied. As the structure resonates, the tip mass moves up and down, which in turn applies a strain on the PZT device in the "1" direction (lengthwise along the beam). This strain induces a voltage in the "3" direction, or from the top to the bottom of the beam. Because the voltage is generated in the "3" direction and the strain is

applied in the "1" direction, it is called d_{31} mode of operation. This is less efficient than d_{33} mode of operation, but still advantageous because of the resonant structure of the beam [8].

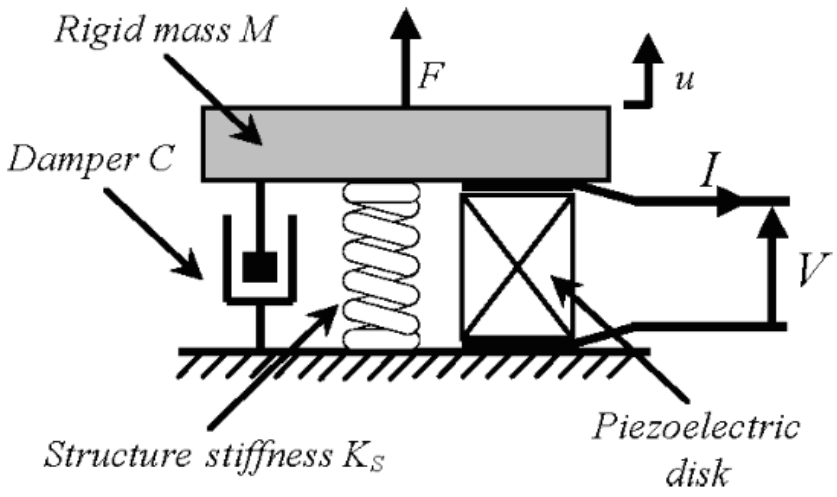

Figure 2.2 Schematic representation of the electromechanical model [9]

The configuration shown in Figure 2.1 creates a mass spring damper system, for which many models have been proposed [9-14]. Treating the system as a mass-spring damper system yields a schematic representation such as the one shown in Figure 2.2. This system consists of a rigid mass *M*, a damper *C*, a spring with stiffness Ks representing the structure system, and a piezoelectric modeled as a spring with stiffness K_P and a voltage controlled force generator αV. A force F is then applied in the shown direction causing a displacement u in the shown direction. The PZT is assumed to have an output capacitance C_p. This model is described by (2.1) and (2.2), a system of linear equations with a form not different from the form that describes RLC circuits.

$$M\ddot{u} + C\dot{u} + \left(K_e + K_p\right)u + \alpha V = \boldsymbol{F} \tag{2.1}$$

$$-\alpha u + CpV = -I \tag{2.2}$$

This model is useful for providing information on directly related to the displacement, velocity and acceleration of the rigid mass. It also allows for easy calculations of instantaneous energy stored in the cantilever due to the stiffness of the beam and displacement of the mass, as well as stored electrically on the capacitor, making it an effective model for describing the mechanical phenomena related to a PZT cantilever. Unfortunately, this model does not, at first glance, provide insight into the electrical impedance of the cantilever, or how to properly match the cantilever.

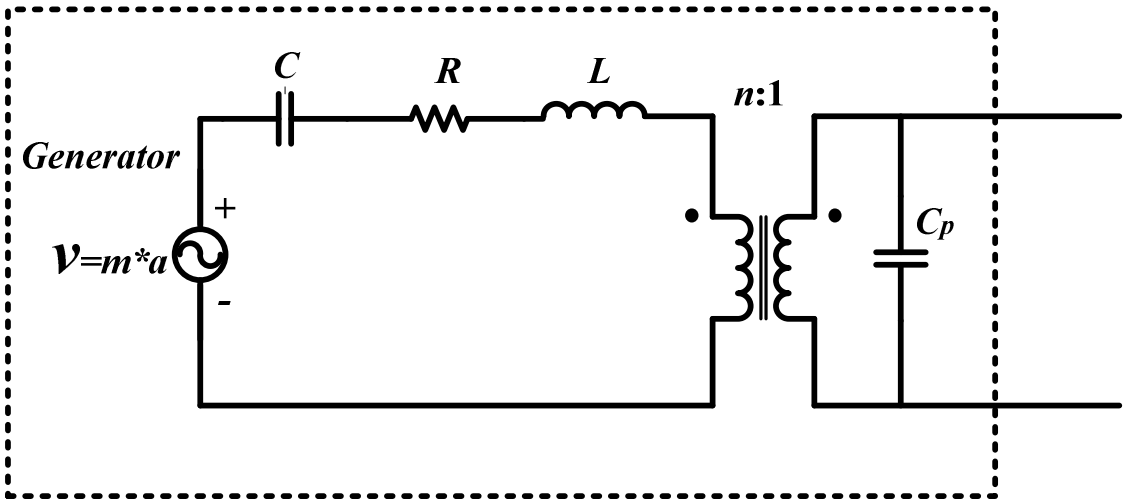

Figure 2.3 Electrical model for PZT cantilever [13]

Mass spring damper systems are linear systems that act similarly to RLC tanks. Because of the form of (2.1) and (2.2), it is possible to redraw the mass spring damper system as an RLC tank, with a transformer representing the electromagnetic coupling. Figure 2.3 shows the circuit that was derived by Elvin et al. [13], using the mechanical model shown above. the voltage generated is proportional to the force exerted on the cantilever, while the series capacitance is

proportional to one over the sum of the cantilever stiffness K_e and the PZT stiffness K_p, while the series resistance is proportional to the damping C, the series inductance is proportional to the mass *m* and the turns ratio *n* is proportional the coupling coefficient α. Because Cp already represented a real capacitance, the value remains the same. When looking at this model, the mechanical energy is described on the left side of the transformer, and the electrical energy is described on the right side of the transformer. The transformer itself represents the electromechanical coupling, changing energy from mechanical to electrical and back from electrical to mechanical.

Examining the electrical model in Figure 2.3 provides insight into a number of phenomena. Firstly, the voltage source is proportional to force, or mass times acceleration. This means that increasing the will increase the power generated, which is not surprising because that corresponds to larger vibrations. It also implies that a heaver mass under the same acceleration generates more energy. Secondly, the mechanical device is not lossless; the mechanical damping (corresponding to the resistor) will cause a loss of energy.

The resonant frequency is important for PZT cantilevers, as the cantilevers are only capable of harvesting significant energy near their resonant frequency. The series inductance and capacitance will define the resonant frequency, which is known to be $\frac{1}{\sqrt{LC}}$. Using this knowledge while examining the model, we can see that raising the mass of the cantilever decreases the resonant frequency, while increasing the stiffness of the structure will increase the resonant frequency.

The last important information to extract from this is that energy not only flows from the mechanical side to the electrical side, it can flow back from electrical energy into mechanical

energy. This means that the electrical load Z that is connected will affect the physical motion of the cantilever. Carefully choosing a reactive load Z is even capable of changing the mechanical resonance of the PZT cantilever.

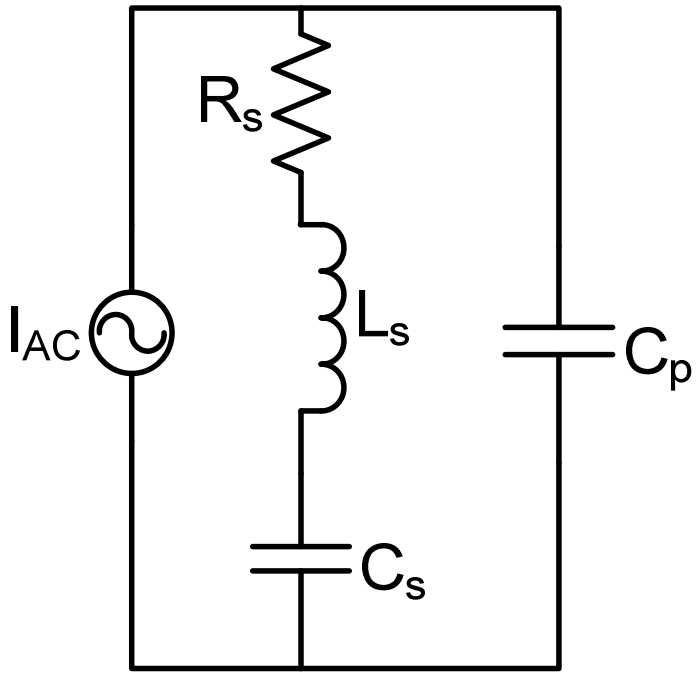

Figure 2.4 Proposed electrical model for PZT cantilever

$$Rs = \frac{R}{n^2} \tag{2.3}$$

$$L_s = \frac{L}{n^2} \tag{2.4}$$

$$C_s = n^2 C \tag{2.5}$$

$$I_{AC} = \frac{\frac{V}{n}}{R_s + sL_s + \frac{1}{sC_s}} \tag{2.6}$$

For purposes of analyzing the input impedance, it may be desirable to completely remove the transformer, and define an equivalent Thevenin or Norton source impedance. This may be

done by reflecting the series RLC and voltage source on the left side of Figure 2.3 to right side. The impedance from RLC gets divided by n^2, while voltage V gets divided by n. Next, it is possible to do a Norton equivalent transformation on the, yielding a circuit in the form of Figure 2.4, with new values shown by (2.3)-((2.6)

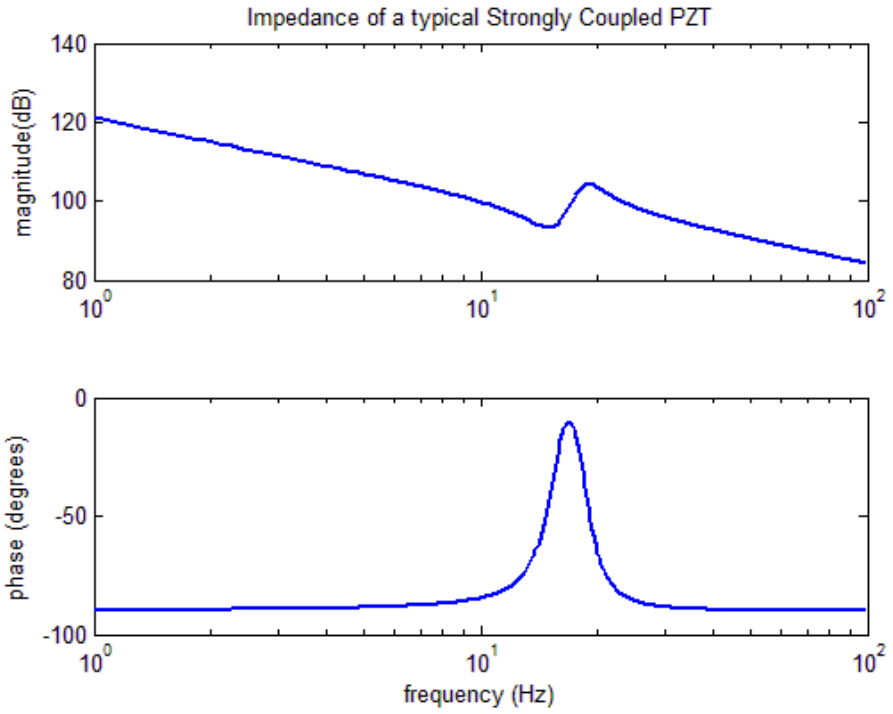

Figure 2.5 Impedance of a typical strongly coupled PZT

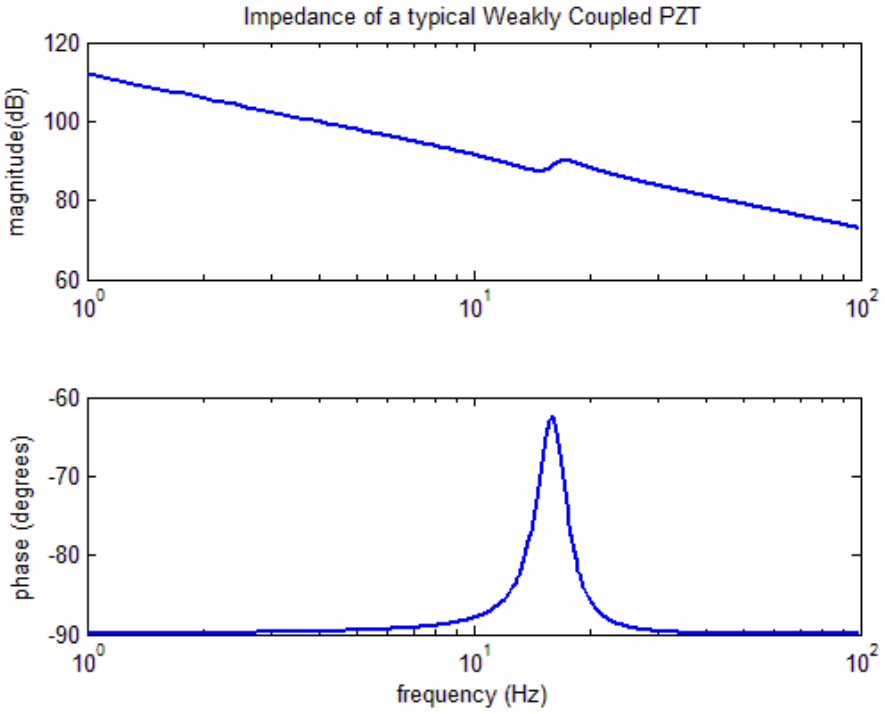

Figure 2.6 Impedance of a typical weakly coupled PZT

This model is advantageous because it gives an easily defined and intuitive representation of the source impedance of the PZT device, and its energy. It is disadvantageous for those wishing to calculate mechanical parameters, as the components no longer easily relate exactly to the mechanical parameters. It is also important to note that as a result of the equivalent Norton transformation, I_{AC} is not directly proportional to the force applied, even though the previous Voltage was. I_{AC}, as can be seen in ((2.6), is now a function of force applied and the frequency of excitation.

Using this model, it is possible to obtain the impedance of a typical PZT cantilever. Based on the coupling coefficient, there are different characteristics that a PZT cantilever can take, and different matching techniques needed [15]. Strongly coupled PZTs have a high coupling coefficient, and as a result the parallel capacitor C_p does not contribute as much at the

resonance, yielding nearly pure resistive source impedance near resonance. The impedance of a strongly coupled PZT can be seen in Figure 2.5. Weakly coupled PZTs see a larger effect of the parallel capacitance C_p near resonance, and is not purely resistive even near resonance. The impedance of a weakly coupled can be seen in Figure 2.6.

Examining Figure 2.5 and Figure 2.6, it is now possible to draw some conclusions about the source impedance. The first obvious thing is that for most frequencies the source impedance has a phase of -90 degrees. This corresponds to current and voltage completely out of phase, and will not deliver any energy. Physically, this means that it is difficult to harvest energy from frequencies far from resonance.

For simplicity, this thesis provides all numbers and values based on the same PZT model. This is the PZT which is shown in Figure 2.6, and is a weakly coupled PZT. A weakly coupled PZT was chosen due to the large improvements which can be seen from reactive matching. Using the model from Figure 2.4, the PZT model has the following values: R_s is 56.4kΩ, L_s is 2.592kH, C_s is 40.15nF, and C_p is 358.8 nF. Note that R_s C_s and L_s are not electrical components, but models that represent the mechanical parameters.

2.2 Maximum Power Transfer Theorem and Implications

For purposes of impedance matching, it is desirable to express the power transfer in a generalized form. This section shows a generalized form for power transfer given that the input impedance of the next stage can be described as a linear system.

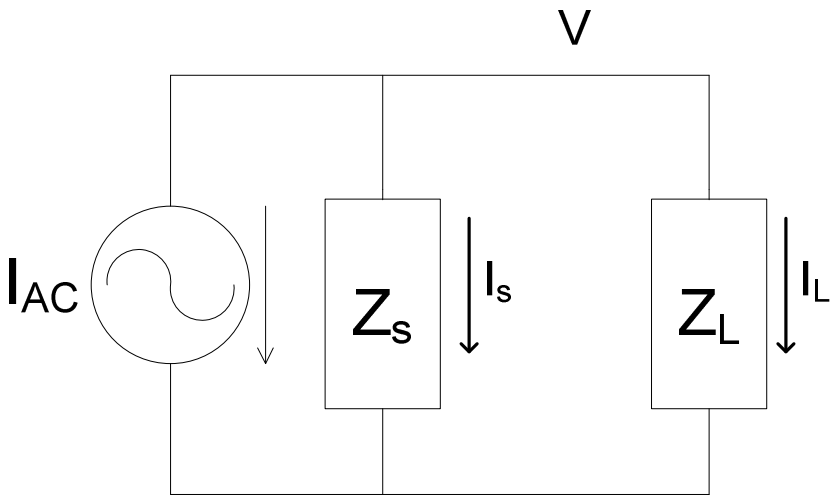

Figure 2.7 General model for source impedance and load impedance

Figure 2.7 shows a general model for the Source and Load impedances of a linear PZT harvesting scheme. Assuming that at each frequency, the impedance can be written in the form of $Z_s(\omega) = R_s(\omega) + sX_s(\omega)$, and in the form of $Z_L(\omega) = R_L(\omega) + sX_L(\omega)$ it is possible to express the power delivered to the load at any frequency normalized to the magnitude of the excitation from the current source.

$$\frac{P_L(\omega)}{|I_{AC}(\omega)|^2} = \frac{\frac{1}{2}R_L(\omega)}{(R_s(\omega) + R_L(\omega))^2 + (X_s(\omega) + X_L(\omega))^2} \tag{2.7}$$

Using (2.7) it is possible to determine the ideal match at any frequency determines when $X_s = -X_L$ and when $R_s = R_L$, corresponding to a complex conjugate match. Looking at Figure 2.5 and Figure 2.6, we can tell that the reactance X_s is always negative, so it is theoretically possible to match the PZT at any frequency using an RL match. In reality, the model becomes slightly more complex far away from resonance, and it has only been demonstrated that this can be done very close to resonance [16].

While it is possible to match at any frequency with an inductor, the size of the physical inductor required to match is quite prohibitive. Depending on the PZT, the required inductor can be anywhere from 10 H up to thousands of Henries. This makes using an actual physical inductor impractical.

$$R_L(\omega) = \sqrt{R_s^2(\omega) + X_s^2(\omega)} \tag{2.8}$$

Due to simplicity of implementation, as well as low power consumption, many researchers have proposed harvesting using purely resistive input impedance. This can be effective when the reactive terms are about the same size as, or smaller than the resistive terms. In terms of the equations this is equivalent to trying to achieve the best match given the constraint $X_L = 0$. By taking the partial derivative of (2.7) with respect to the load resistance, and setting the result equal to zero it is possible to show that ((2.8) gives the ideal load resistance for a purely resistive match. It should be noted that both the source resistance and source impedance are functions of frequency for a PZT cantilever, so each frequency will have a different ideal resistive match. It is also to note that the PZT voltage is frequently full-wave rectified before matched with the resistive impedance, which will add some unintended effects.

Table 2.1. Power transfer for ideal resistive and RL matches as a function of frequency

f(Hz)	R match (kΩ)	L Match (H)	Power (mW)	R only Match (kΩ)	Power mW
12	2.356	395.0529	1	29.879	0.1462
13	3.387	324.1357	1	26.692	0.2252
14	5.285	267.7383	1	24.137	0.3593
15	8.757	232.2017	1	23.571	0.5417
15.9	12.496	238.8464	1	26.935	.6338
16	12.743	242.3783	1	27.498	0.6333
17	10.996	276.4713	1	31.512	0.5174
18	6.209	264.9329	1	30.6	0.3374

19	3.346	234.0731	1	28.143	0.2125
20	1.942	205.366	1	25.88	0.1396

Table 2.1 shows the power transfer for a typical weakly coupled PZT as a function of frequency, with the same base acceleration. It can be seen that the inductance values required for an RL match are unreasonably large for a small system of traditional passive components. As can be seen, at any frequency the ideal RL match is theoretically capable of extracting maximum power at any frequency, while the pure resistive match works very well near the resonant frequency of 15.9 Hz. Note that the ideal match impedance is a function of frequency, and no single match obtains the most power at any one frequency.

Real vibration sources rarely provide a single frequency of vibration [17-21]. In the real world, the frequency spectrum of vibrations is irregular, and constantly changing. This makes optimal power extraction a difficult problem, but systems which can provide good power extraction at multiple frequencies (various techniques of this are discussed later) will perform better than systems that cannot.

2.3 Typical Power Management Circuit

A typical Power Management Circuit (PMC) for a PZT cantilever consists of 3 separate stages, all of which may function together. While some specialized harvesters may combine or omit multiple stages, the bulk of existing PMC today follow this basic technique.

Figure 2.8 shows the block diagram for a typical PMC designed for PZT cantilevers. The first stage is a rectification, which is responsible for turning the AC electrical energy from the PZT to DC electrical energy. The simplest rectification scheme is a full-bridge rectifier, such as the rectifier shown in Figure 2.8. In some systems, diodes may be lossy, unavailable, or

disadvantageous. Various active or passive configurations of MOSFETs may be used to implement diodes or diode bridges, as discussed in detail in Section 3.

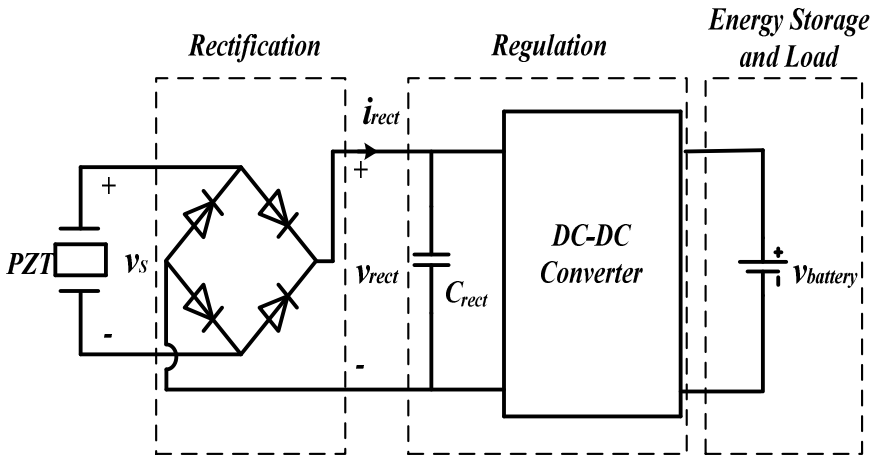

Figure 2.8 Block diagram for typical PMC

The second stage for a typical PMC is the regulation stage. Regulation circuitry is implemented with a wide array of strategies, goals and designs, but typically uses DC-DC converters with varying control logic for implementation. The three most common types of DC-DC converter are step down (buck) converters, step up (boost) converters, or step up/down (buck-boost) converters.

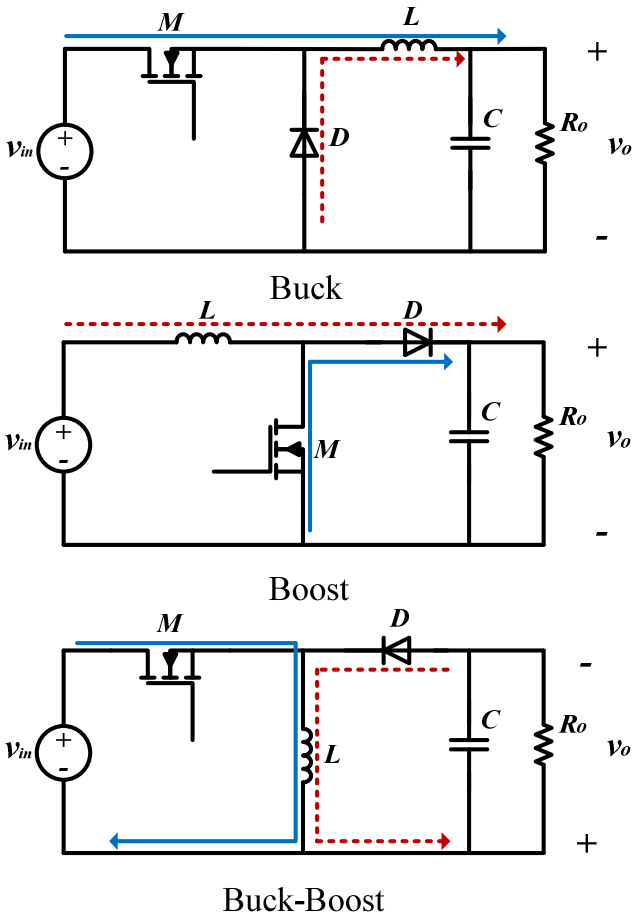

Figure 2.9 Current paths for the three most common DC-DC converters

A diagram for the three most common switching converters can be seen in Figure 2.9. The current paths for the on time, D, where the switch is closed and the inductor is charging are marked by the solid blue lines. Current paths for the off time, D', while the switching is open and the inductor is discharging into the output are shown by the dotted red lines. These converters are very well explored, although novel control circuitry can still be imagined to give them new uses in different applications.

Traditional power regulation circuits regulate an output voltage, and allow the input voltage to change as it will. These circuits are sometimes used for vibration energy harvesting purposes, and are advantageous because they relax the constraints on the energy storage and

load, allowing a simple capacitor to be used. These systems are disadvantageous because there is no regulation being performed on the input voltage and currents. This means that the system may achieve a very poor match with the PZT source impedance, failing to extract the maximum achievable power.

Often times the goal of a vibration energy harvesting circuit is to charge a battery. In these systems, the battery effectively regulates the output voltage, allowing the regulation circuit to regulate the input voltage. By regulating the input voltage, it is possible to design the control circuitry such that the goal is to match to the PZT, or in some way extract maximum power. There are various techniques to do this, including pure resistive matches, reactive RL matches, and some non-linear matches, all of which rely on the control circuitry of the regulation circuit for implementation. Because there are a variety of these techniques, and they tend to extract more power, and they are the focus of the remainder of this thesis.

The final stage of a typical PMC is the energy storage and load. In general, energy storage consists of a capacitor which requires output regulation, a battery which does not, or a super capacitor, which requires special considerations. Various loads have been envisioned for PZT cantilever based energy harvesting, and can be changed based on application.

2.4 Past Approaches

The following is a survey of previous approaches, and an analysis of the advantages and disadvantages of existing systems. Examples are given of various energy harvesting schemes and systems.

2.4.1 Resistive Matches

The simplest kind of PZT matching is a pure resistive match. While, in most cases, they do provide optimized power output, they are simple, can be implemented with low power components, and provide a reasonably well matched configuration. A number of researchers have investigated static resistive matching due to its efficiency with relatively simple implementation [22-24].

If a resistive match is desired only at a single frequency (resonance matches are by far the most common), then a static resistive match is needed. Using a buck or buck-boost converter, it is possible to implement a switching converter with pure resistive input impedance using an open loop controller.

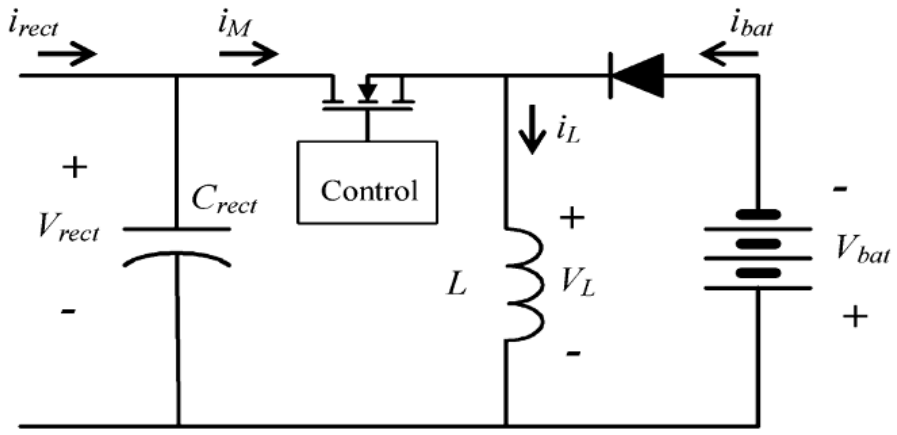

Figure 2.10 Buck-Boost with constant input impedance [22]

$$R_{in} = \frac{V_{Rect}}{i_{rect}} = \frac{2L}{D^2T} \tag{2.9}$$

Figure 2.10 shows an example of a buck-boost converter with open loop control and constant input impedance. The converter operates in Discontinuous Mode (DCM) with a PWM of constant frequency and a variable duty cycle determined by the PI controller. Because the battery controls the output voltage, there is no need to regulate the output voltage, and the PWM

sent to the gate of the MOSFET controls the input current. It has been shown that for a buck-boost in this configuration, the input impedance can be given by (2.9), as derived by Kong et al. [24].

Because the ideal matching resistance is not constant, and varies as a function of frequency, there has also been a body of research related to dynamic resistive matches, that try to change the input impedance of the converter based on the excitation frequency [23, 25-27]. These topologies provide a better match, at the expense of complexity, and in general higher power consumption

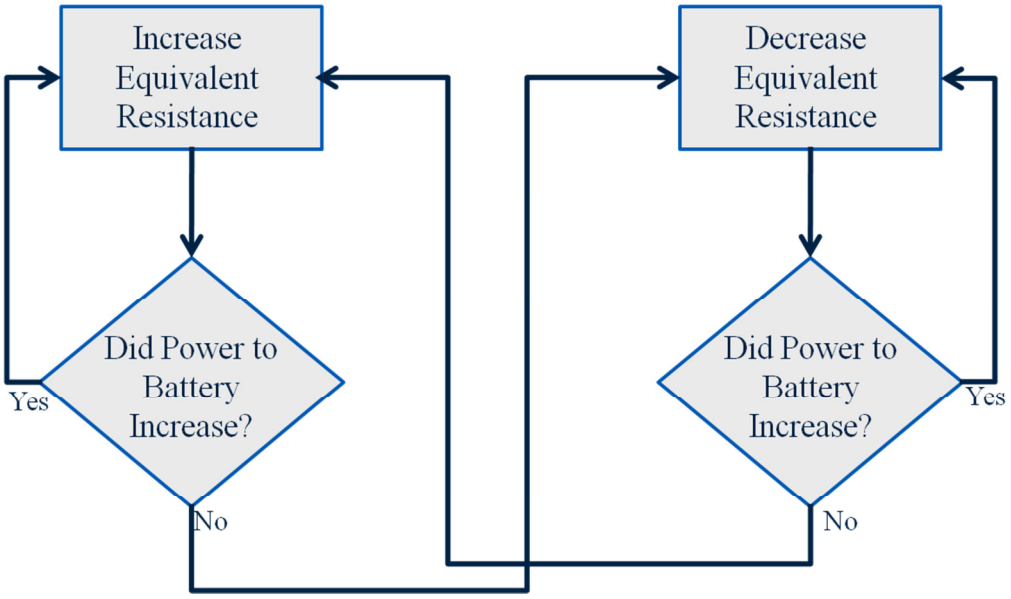

Figure 2.11 General form of perturb and observe algorithm

While there are varying methods of tracking the resistance that yields maximum power, perturb and observe (also called "Hill Climbing) is probably the simplest and most commonly used. Figure 2.11 shows how the “perturb and observe” algorithm typically operates. The general idea is to change the input resistance, and compare the new power to the old power. If

power is increased, the resistance continues changing in the same direction, if the power is decreased, the resistance changes in the other direction.

2.4.2 Non-Linear Matches

Due to the difficulty of implementing a good RL match, many researchers have proposed non-linear matching techniques for harvesting energy from PZTs. These techniques tend to rely on manipulating the charge stored on the output capacitor C_p, through use of well-timed switches. This can be useful, because the when the voltage across the PZT is positive and decreasing (or negative and increasing), the energy from the PZT is wasted to discharge the capacitor. The two common non-linear matching techniques for PZTs are Synchronous Switch Damping (SSD) and Synchronous Switch Harvesting Inductors (SSHI).

Synchronous switch damping is a non-linear PZT energy regulation technique that relies on extracting all power from the output capacitance when it reaches its peak voltage [28-30]. When compared to a linear resistive match, this has been shown in one case to increase power extraction by as much as 400% [30].

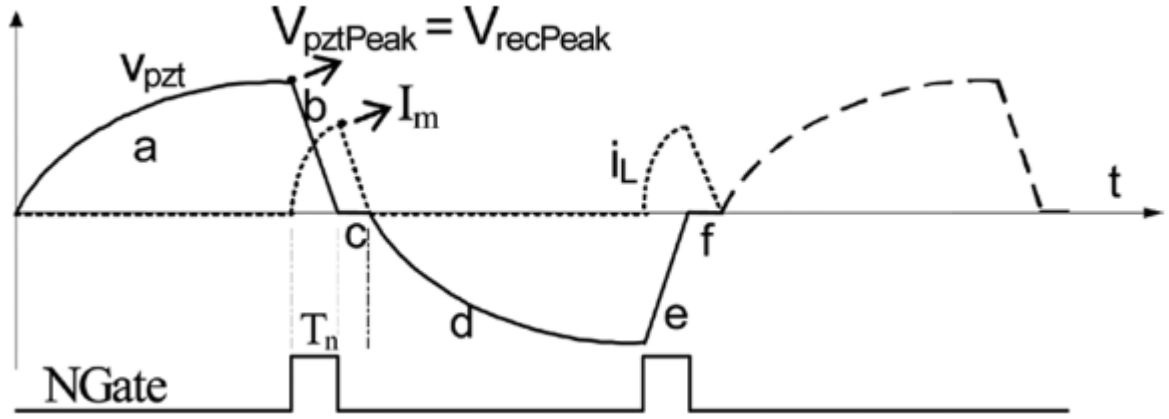

Figure 2.12 SSD converter control timing [29]

Figure 2.12 shows the timing diagram for an example SSD converter, which was implemented using a buck converter (although this technique is readily usable for buck-boost or flyback topologies). There is a full wave rectifier before the buck converter, so that the AC voltage can be harvested. The switching converter remains inactive for long periods of time (approximately half the PZT excitation frequency), while sensing the PZT voltage. When the converter senses the peak PZT voltage, it drains all energy off of the capacitor, reducing the wasted energy to discharge the capacitor, and allowing it to quickly being charging in the opposite direction.

SSHI is a non-linear rectification technique, also sometimes called a "Bias-Flip Rectifier," that relies on a switch and an inductor to flip the voltage across the output capacitance C_p [31-34]. When compared with standard matching techniques, it can be shown that SSHI can increase energy harvested by up to 900% [34].

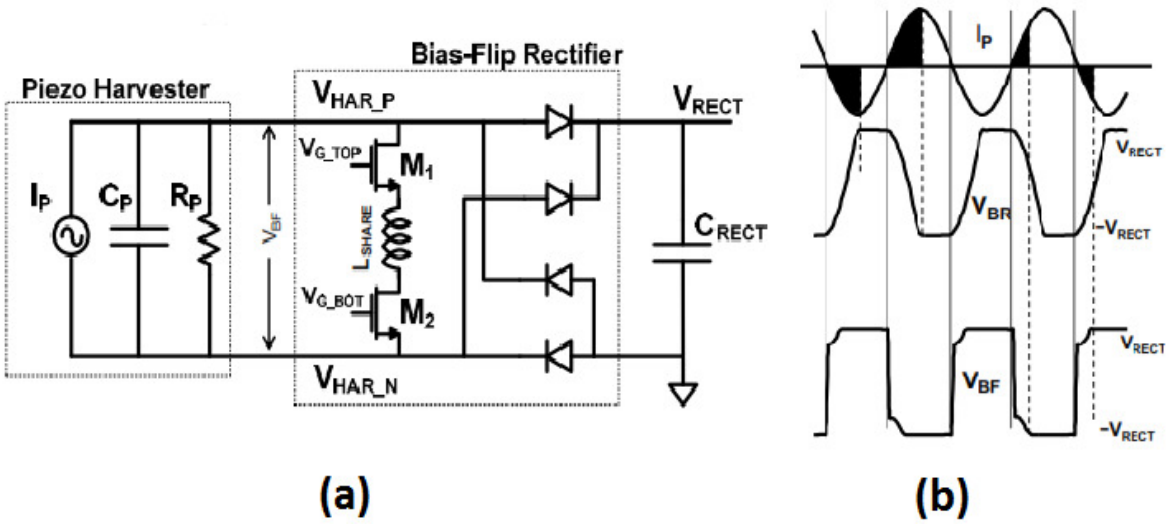

Figure 2.13 (a) Typical SSHI rectifier and (b) Typical switching waveforms for typical full-bridge rectifier and SSHI rectifier [32]

Figure 2.13 (a) shows the schematic for a typical SSHI topology. M1 and M2 form a "bi-directional" switch, and are always both "on" or "off" but can block current in either direction when off. The idea behind the bi-directional switch and the inductor is that when M1 and M2 are turned on for a short period of time, the voltage on the output capacitor C_p is flipped, preventing the need to spend harvestable energy discharging the capacitor.

Figure 2.13 (b) shows the PZT output voltage for a typical rectifier V_{BR} and an SSHI rectifier V_{BF}, when considering the excitation current I_p. Current is only delivered to the load when the PZT output voltage is equal to V_{rect} plus the necessary diode drop. As can be seen, the typical rectifier waveform V_{BR} wastes some current from IP (highlighted in black for the first switching period) while changing the capacitor voltage. By using the bi-directional switch and flipping the capacitor voltage right as the sign of the current changes, it is possible to decrease the wasted current. Looking at the PZT output voltage VBF of an SSHI system, it can be seen that the wasted current (shown in black for the second switching cycle) is significantly lower.

Non-linear harvesting techniques typically harvest more energy than traditional resistive matches. The trade-off is that the control is more complicated, and requires accurate peak or slope detection circuitry, which consumes a relevant amount of power in many low-power systems.

2.4.3 Reactive Matching

As discussed earlier, an RL match is capable of delivering maximum power at any given frequency. RL matches are not used with passive components, because they have prohibitively large capacitances (100s of H for our example PZT), and provide unregulated AC power to the resistive load, which is not useful in most modern electronics. Saggini et al. [16] have proposed a

switching converter capable of showing a user-defined complex input impedance, and demonstrated that this technology can be used to match PZTs.

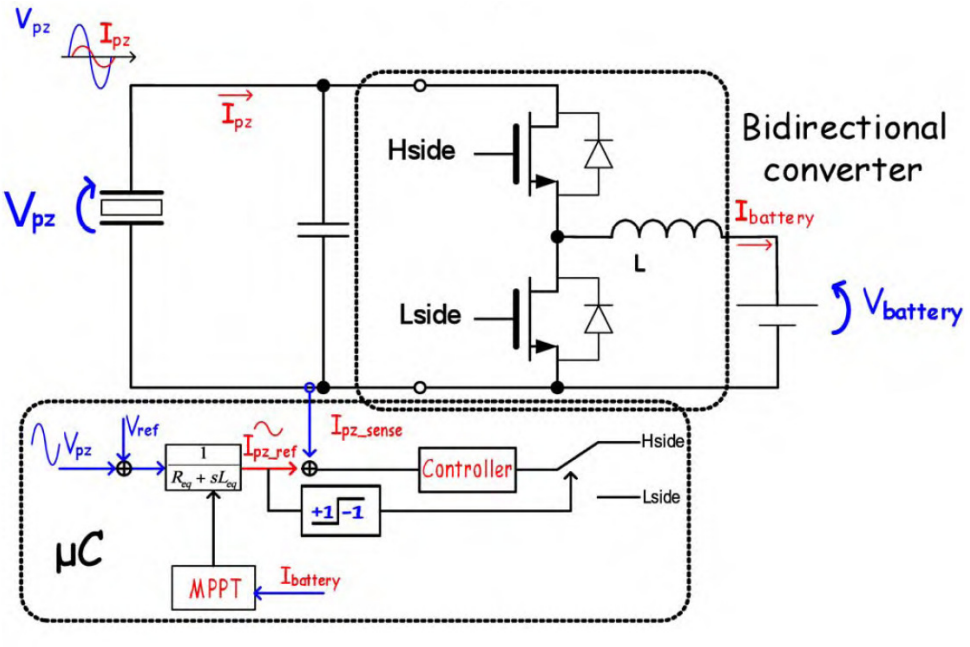

Figure 2.14 Schematic of proposed reactive match [16]

Figure 2.14 shows the proposed schematic of the circuit proposed by Saggini et al. [16]. The switching converter is a Bidirectional DC-DC converter. This converter requires that the input is kept at a higher voltage that the output, and is capable of bucking current from the input to the output, or boosting current from the output to the input. This converter is analyzed in depth in Chapter 3.

The output voltage is clamped by a battery, allowing the control circuitry to regulate the input voltage and current. To emulate the desired input impedance, a feed-forward loop senses the PZT voltage, and multiplies by the ideal admittance (an RL match in this case), yielding the ideal current. This current is compared to the actual current, and the error signal is sent through a PI controller. In this way, the actual PZT current is forced to what it would be if matched with

the imaginary RL circuit. If current should be flowing into the RL match, the buck circuit is active, taking current form input to output. Similarly, when the current should be flowing out of the RL match, current is boosted from the battery to the PZT.

In order to provide a wider band match, the topology performs a two dimensional MPPT algorithm to track ideal resistance and the ideal inductance for changing excitation frequencies. This is done using a digital controller, which senses the average battery current, and uses a method similar to perturb and observe, in two dimensions to converge to the ideal R and L values based on maximizing the current to the battery. Two dimensional MPPT theoretically allows maximum power extraction at any frequency, but is power intensive (as it requires digital control), and can fail to track maximum power if there are local maxima which may be caused by noisy or irregular vibration sources, which are common in real world applications. The results also showed that power harvested away from resonance was small, even when ideally matched, implying that real systems cannot be matched far away from the mechanical resonance.

This method is advantageous when compared with the other methods, as it provides maximum power extraction, through use of an RL match. The complexity and power consumption of a system like this is restrictive, and must be designed with care in order to provide better system performance.

2.5 Proposed Approach

The approach proposed by this paper is an expansion on the work done by Saggini et al. [16]. A fully analog implementation is explored in order to reduce power consumption. Because RL matches away from resonance are not as effective, this work focuses on a single, static, reactive match for a PZT cantilever at the frequencies around resonance. The novelty of this

approach is the input impedance, which is not a conventional RL match, but a complex system of poles and zeroes that can shape the input impedance of the converter, to provide a better match than a traditional RL match.

$$Y_{in}(s) = \frac{K}{s}\frac{\left(\frac{s}{\omega_{z1}}+1\right)\left(\frac{s}{\omega_{z2}}+1\right)}{\left(\frac{s}{\omega_{p1}}+1\right)\left(\frac{s}{\omega_{p2}}+1\right)} \tag{2.10}$$

The chosen input impedance is shown in (2.10). This admittance was chosen because the poles and zeroes allow the impedance to be shaped according to the PZTs source impedance. Further, while this is appears to be a complicated impedance with many poles and zeroes, it can be implemented with a single op-amp, allowing for a low power analog implementation and the exact implementation is discussed in chapter 3. This thesis will use theoretical calculations and simulation results to show that a converter can be implemented with that input impedance in a fully analog fashion, and extract the power that would be expected, which is higher than that of a traditional RL match.

3: Proposed Match and Topology

This section will present the block diagram of the proposed topology, and purpose of each block. An in depth analysis of operating parameters and necessary design for each block is then discussed.

3.1 Block Diagram of Proposed System

The system proposed system has operation principles very similar to the converter that was proposed by Saggini et al. [16]. The primary differences are that there is no longer MPPT

circuitry, the circuit is implemented in a fully analog fashion, and the ideal input admittance is a complex system of poles and zeroes.

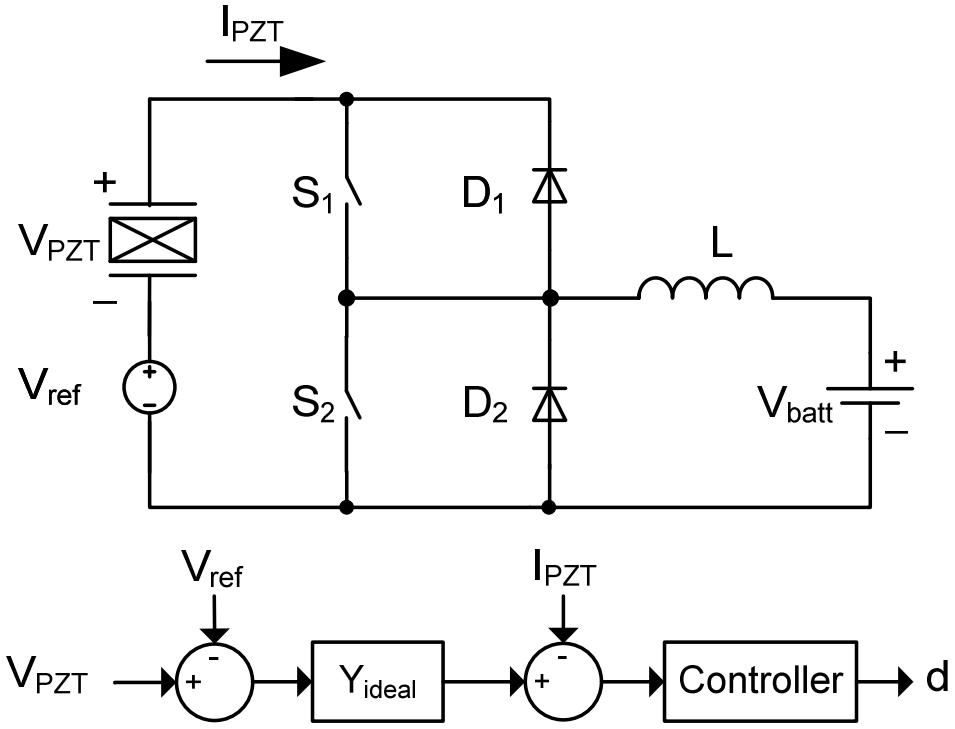

Figure 3.1 Block diagram of proposed system

A block diagram describing the overview the system can be seen in Figure 3.1. The battery clamps the output to the desired voltage, allowing for control signals to control input voltages and currents. Applying a PWM to S_1 will buck current from PZT to battery, while applying a PWM to S_2 will boost current from battery to PZT.

The feed-forward loop first injects a DC offset, V_{ref}, which is discussed in section 3.2. Next, the ideal input admittance given in (2.10) multiplies the PZT voltage, giving the ideal PZT current. This is compared to the actual PZT current, and a PI controller controls the Duty cycle. A comparator (which is not shown) compares the ideal PZT current to zero, in order to determine if a PWM should be applied S_1 or S_2.

3.2 Input Offset

One of the main challenges of harvesting energy from a PZT is converting the AC energy provided by the PZT into DC energy. AC-DC conversion is typically more complex than DC-DC conversion. Full bridge rectifiers are frequently used (despite the power loss they cause), but because diodes block current that would return to the PZT, preventing the implementation of a reactive match such as the match proposed here. To solve these issues, a DC offset is added to the AC signal generated by the PZT.

The DC offset is added by V_{ref}, as shown in Figure 3.1. Because of the integrating nature of the controller, the reference voltage V_{ref} will become the DC voltage, with the AC PZT voltage oscillating around V_{ref}. From a physical standpoint, this energy is stored on the output capacitor C_p. Saggini et al. [16] have constructed a system that uses a DC offset in this fashion, and confirmed that the PZT operates similar to the model with a DC offset applied, meaning that this can be done without a noticeable penalty.

$$V_{ref} \geq V_{batt} + \frac{V_{pktopk}}{2} \tag{3.1}$$

In order for the converter to stay in its desired operating range, the PZT voltage must remain higher than the battery voltage. This means that the minimum offset voltage can be defined as a function of the battery voltage and the peak-to-peak voltage as seen in (3.1).

The offset voltage is a critical key to the operation converter. Without the offset voltage, complicated AC-DC conversion is required, which tends to have low efficiency and difficult control. With respect to the switching frequency, typical PZT resonances are so slow that the changes can still be handled by DC-DC converters. This means with the addition offset voltage,

efficient DC-DC conversion is implementable on the AC source provided by the DC-DC converter

3.3 Bidirectional DC-DC Converter and Equations

In order to implement the desired input impedance, an appropriate power converter must be chosen. This thesis will focus on the bi-directional DC-DC converter which is shown in Figure 3.2. The bi-directional converter was chosen because of its ability to source or sink current to and from the load. This is necessary because when emulating complex input impedances with AC currents, it is possible that power will need to flow from the battery to the PZT, in addition to flowing from the PZT to the battery.

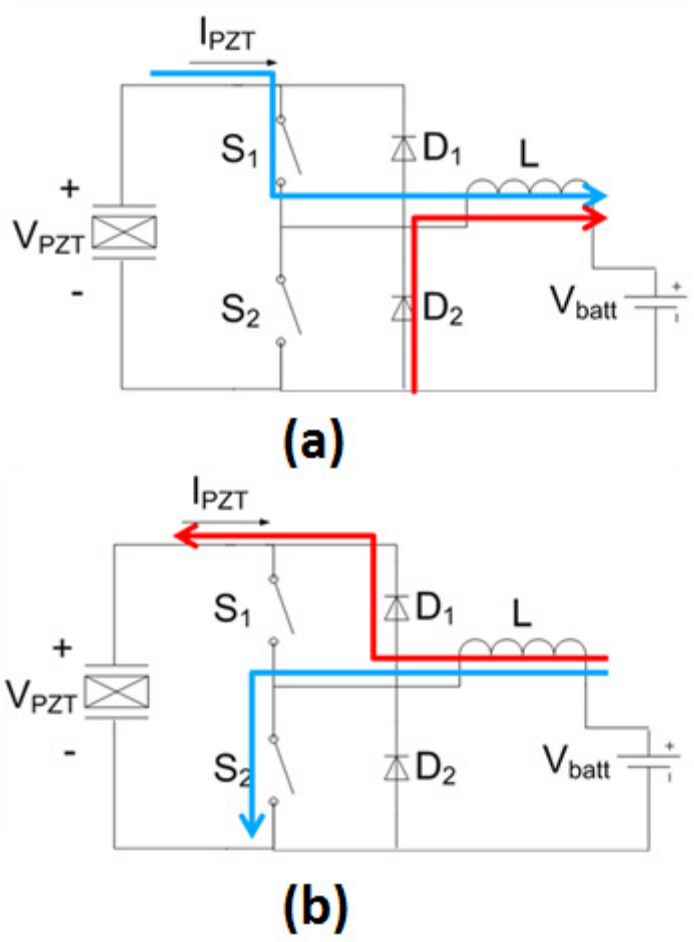

Figure 3.2 (a) Current paths for buck mode and (b) current paths for boost mode.

Figure 3.2 (a) shows the bi-directional DC-DC converter while in "buck-mode." In this mode, current is transferred from the PZT to the battery, and a PWM is applied to S1, and the current is controlled by the duty cycle and frequency of this PWM. When the switch is closed, the current path is from the PZT through S1, through the inductor to the battery, shown in blue. When the switch is open, the current path is through D2, the inductor and into the battery, shown in red.

Figure 3.2 (b) shows the bi-directional DC-DC converter while in "boost-mode." In this mode, current is transferred from the battery to the PZT, and a PWM is applied to S2, and the

current is controlled by the duty cycle and frequency of this PWM. When the switch is closed, the current path is from the battery, through the inductor and S2, shown in blue. When the switch is open, the current path is from the battery, through the inductor and D1, into the PZT, shown in red.

Using proper control of a PWM, it is possible to generate any current, to or from the PZT, allowing for complex input impedance to be emulated.

3.3.1 Assumptions Required for Analysis

For this thesis, it is assumed that the bi-directional DC-DC converter always operates in DCM. By proper choice of the frequency, and inductor size, based on the range of PZT and battery voltages, this is a valid assumption, and should not cause problems.

For the bi-directional DC-DC converter to operate in either buck or boost mode, it is necessary for the PZT voltage to be higher than the battery voltage. As the PZT voltage is typically and AC voltage, this can be problematic. Because the PZT input is typically an AC voltage, this can be problematic. In order to keep the PZT voltage higher than the battery voltage, it is necessary to add a DC offset voltage to the signal that is at least as high as (3.1), given the maximum peak voltage (V_{pk}). For the analysis, it is assumed that the PZT voltage is always higher than the battery voltage, and that (3.1) holds

In order to perform analysis, it must be assumed that the input current is a DC value, when in reality it is changing. This assumption is valid, as the switching frequency is quite high when compared to the excitation frequency, and the output capacitance of the PZT low pass filters in changes to the voltage. Small differences may be observed due to the small non-linearity introduced by this effect.

3.3.2 Average Input Current Analysis

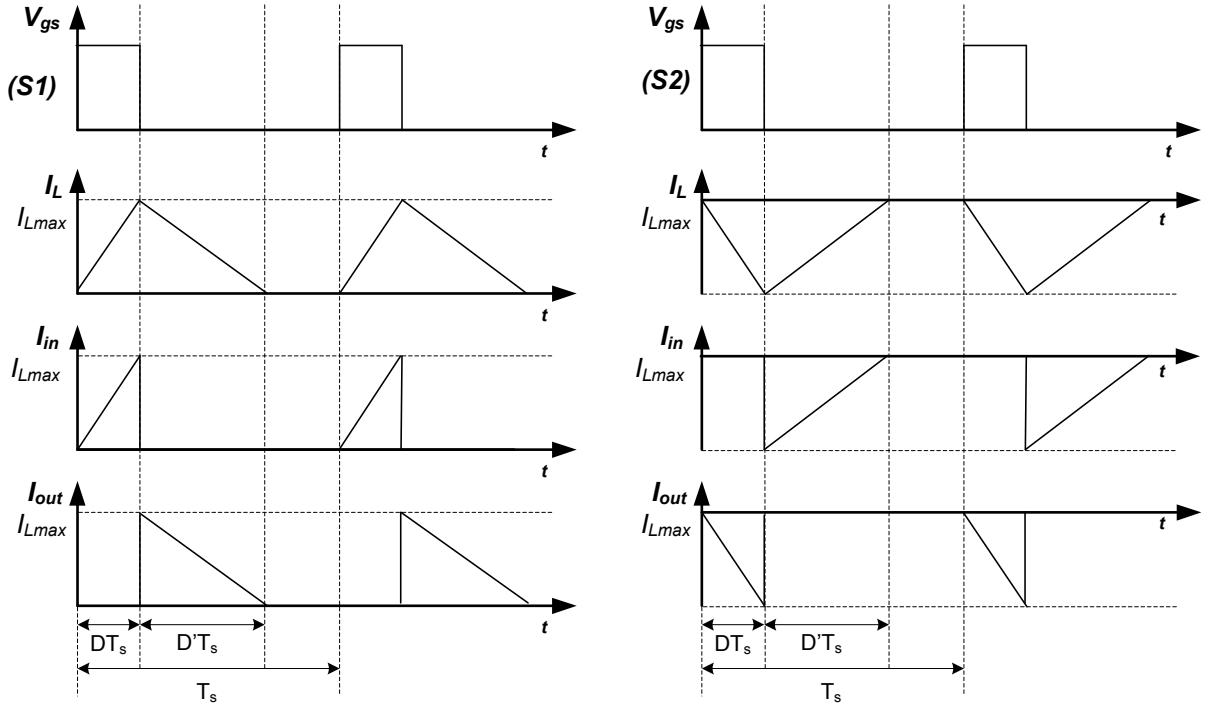

Figure 3.3 Typical switching waveforms for bi-directional DC-DC converter

Figure 3.3 shows the current and voltage waveforms for the PZT voltage waveforms of the bi-directional DC-DC converter in both buck and boost Mode. Using these figures it is possible to derive the relationship between input current, input voltage, and Duty Cycle. Losses are neglected during this analysis.

$$I_{PZT} = \frac{I_{pk}D}{2} \tag{3.2}$$

Figure 3.2 (a) shows the current and voltage waveforms in Buck Mode. Using this and geometry factors, (3.2) can be obtained for buck mode, where I_{pk} is the peak input current, and D is the duty cycle

$$I_{pk} = \int_0^{DT_S} \frac{(V_{PZT} - V_{batt})dt}{2} = \frac{DT_s(V_{PZT} - V_{batt})}{2} \tag{3.3}$$

$$I_{PZT} = \frac{(V_{in} - V_{batt})D^2T}{2L} \tag{3.4}$$

It is possible to obtain I_{pk} by examining the current path seen in figure 1 (a). (3.3) shows the peak current in buck mode where T_s is switching period, V_{PZT} is the PZT voltage and V_{batt} is the battery voltage. Combining terms yields (3.4) the average input current for buck mode.

$$I_{PZT} = -\frac{I_{pk}D'}{2} \tag{3.5}$$

Figure 3.2 (b) shows the current and voltage waveforms in boost mode. Using this and geometry factors, (3.5) can be obtained for buck mode, where I_{pk} is the peak input current and D' is the duty cycle in which current flows through the diode (shown in Figure 3.2 (b).

$$I_{pk} = \int_0^{DT_s} \frac{V_{batt}dt}{2} = \frac{DT_s(V_{batt})}{2} \tag{3.6}$$

It is possible to obtain I_{pk} by examining the current path seen in Figure 3.2 (b). After doing so, (3.6) shows the peak current when the converter is in boost mode.

$$D' = \frac{DV_{batt}}{V_{PZT} - V_{batt}} \tag{3.7}$$

$$I_{PZT} = -\frac{V_{batt}^2 D^2 T}{(V_{PZT} - V_{batt})2L} \tag{3.8}$$

D' can be represented in terms of the Duty Cycle, battery voltage, and PZT voltage as shown in (3.7). Combining Terms yields (3.8), the average input current in boost mode.

3.3.3 Small Signal Input Current Analysis

In order to perform small signal analysis on the loop gain, it is necessary to determine how small signal changes to the PWM will effect changes to the current. For this research, a constant frequency PWM is used, and the relevant parameter for AC analysis will be $\frac{\hat{\imath}_{PZT}}{\hat{d}}$, which will be different for both buck and boost mode.

$$\begin{aligned} I_{PZT} + \hat{\imath}_{PZT} &= \frac{(V_{in} - V_{batt})(D + \hat{d})^2 T}{2L} \\ &= \frac{(V_{in} - V_{batt})D^2 T}{2L} + \frac{(V_{in} - V_{batt})D\hat{d}T}{2L} + \frac{(V_{in} - V_{batt})\hat{d}^2 T}{2L} \end{aligned} \tag{3.9}$$

For buck mode, this derivation starts with (3.4) and adds a small signal duty cycle $\hat{d}$, to the duty cycle D, and then observes the small signal current perturbation $\hat{\imath}_{PZT}$. This gives an equation in the form of (3.9).

$$\hat{\imath}_{PZT} = \frac{(V_{in} - V_{batt})D\hat{d}T}{2L} \tag{3.10}$$

$$\frac{\hat{\imath}_{PZT}}{\hat{d}} = \frac{(V_{in} - V_{batt})DT}{2L} \tag{3.11}$$

Using (3.4), the first term can be cancelled with I_{PZT}. The last term is nonlinear ($\hat{d}^2$), and is ignored for analysis, yielding (3.10). From (3.10), (3.11) is trivially obtained.

$$\begin{aligned} I_{PZT} + \hat{\imath}_{PZT} &= -\frac{V_{batt}^2 \left(D + \hat{d}\right)^2 T}{(V_{PZT} - V_{batt})2L} \\ &= -\frac{V_{batt}^2 D^2 T}{(V_{PZT} - V_{batt})2L} - \frac{V_{batt}^2 D\hat{d}T}{(V_{PZT} - V_{batt})2L} - \frac{V_{batt}^2 \hat{d}^2 T}{(V_{PZT} - V_{batt})2L} \end{aligned} \tag{3.12}$$

For boost mode, this derivation starts with (3.8) and adds a small signal duty cycle $\hat{d}$, to the duty cycle D, and observe the small signal current perturbation $\hat{\imath}_{PZT}$. This gives an equation in the form of (3.12).

$$\hat{\imath}_{PZT} = -\frac{V_{batt}^2 D\hat{d}T}{(V_{PZT} - V_{batt})2L} \tag{3.13}$$

$$\frac{\hat{\imath}_{PZT}}{\hat{d}} = -\frac{V_{batt}^2 DT}{(V_{PZT} - V_{batt})2L} \tag{3.14}$$

Using (3.8), the first term can be cancelled with I_{PZT}. The last term is nonlinear ($\hat{d}^2$), and is ignored for analysis, yielding (3.13). From (3.13), (3.14) is trivially obtained. Similar to (3.11), this gain is a constant at a given operating point. It may be noted that the sign is negative, meaning as in

Examination of (3.11) and (3.14) shows that increasing the duty cycle will actually increase the rate at which energy flows from output to input. This negative sign can be handled by inverting the control system, which is discussed later. will be dependent on the PZT voltage, and the duty cycle, both of which will change significantly during operation. For this system to be analyzed, it is assumed that $\frac{\hat{\imath}_{PZT}}{\hat{d}}$ will change very slowly with respect to the switching frequency, so that it may be treated as a range of DC values. This assumption is valid because the excitation frequency (and therefore changes to Duty Cycle and PZT voltage during proper operation) is in the range of 15 Hz, while the switching frequency is 120 kHz.

Even considering $\frac{\hat{\imath}_{PZT}}{\hat{d}}$ as a range of DC values, this parameter complicates the AC analysis, as the changes in the PZT voltage and duty cycle causes $\frac{\hat{\imath}_{PZT}}{\hat{d}}$ to change by more than an order of magnitude. The PI controller (discussed later) must be designed so that it is functional

for a range of $\frac{\hat{\imath}_{PZT}}{\hat{d}}$ values. Note that (3.11) and (3.14) will be revisited in chapter 4, as they are required in order to do a full analysis of the actual input impedance, and loop gain.

3.4 Implementation of Feedback Loop

The control circuitry for the proposed DC-DC converter has been implemented in a fully analog fashion. This section will show the design and implementation of the various blocks required for the operation of the DC-DC converter

3.4.1 Voltage Sense and Input Impedance

The PZT voltage will reach voltages as high as 40V, which is an unreasonably large voltage for micro power op-amps. This voltage must be sensed, and multiplied by the ideal input admittance in order generate the ideal current. This is done with a resistive divider and two op-amps (one as a buffer and one to implement the ideal transfer function).

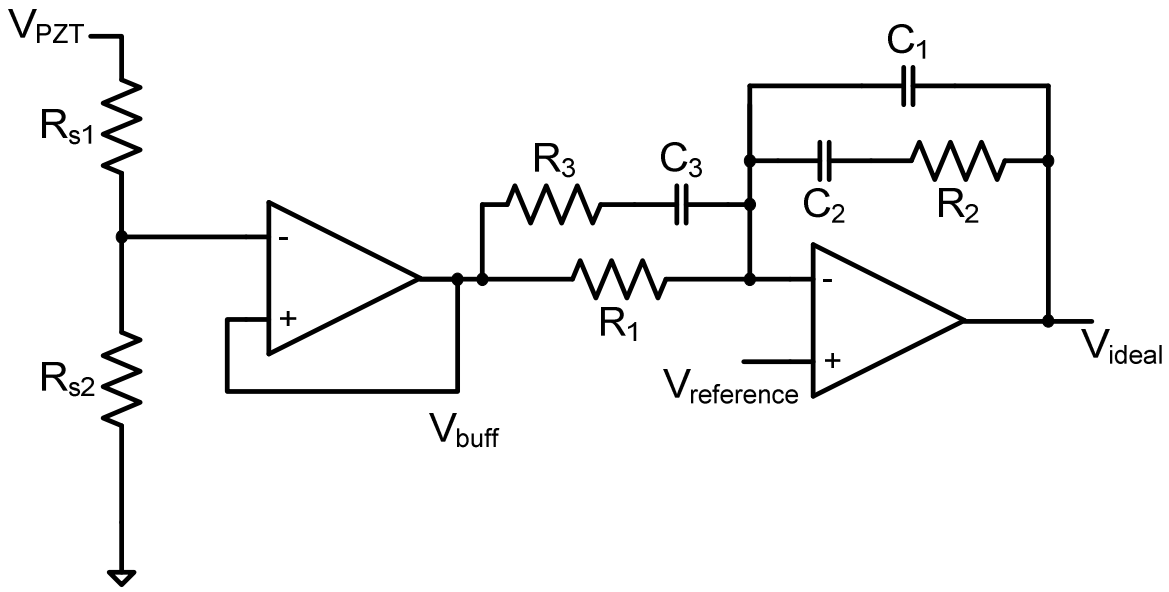

Figure 3.4 Schematic of voltage sense and ideal admittance circuit

Figure 3.4 shows the circuit schematic for voltage sensing, and generation of the ideal current. Because of the high values of the PZT voltage, it is desirable to use a high impedance voltage divider and buffer to sense a fraction of the PZT voltage, instead of directly sensing the PZT voltage. The op-amp after the buffer is used to implement the transfer function for the ideal input impedance, as described by (2.10).

$$\frac{V_{ideal}}{V_{BUFF}} = -\frac{1}{R_1(C_1+C_2)s}\frac{(1+sR_2C_2)\big(1+sC_3(R_1+R_3)\big)}{(1+sR_3C_3)\left(1+\frac{sC_1R_2C_2}{C_1+C_2}\right)} \tag{3.15}$$

$$\frac{V_{ideal}}{V_{PZT}} = -\frac{R_{s2}}{R_{s1}+R_{s2}}\frac{1}{R_1(C_1+C_2)s}\frac{(1+sR_2C_2)\big(1+sC_3(R_1+R_3)\big)}{(1+sR_3C_3)\left(1+\frac{sC_1R_2C_2}{C_1+C_2}\right)} \tag{3.16}$$

Analysis of the op amp shown in Figure 3.4 can be done to show that the transfer function of the op-amp is given by (3.15). Using proper choice of components, it is possible to define any value for the poles, zeros, and the gain. When considering the entire circuit, the transfer function for the entire block can be given by (3.16). Except for the negative sign, it can be easily shown that this equation has the same form as the input impedance that was defined by (2.10), and can be used to generate the ideal current. The fact that this is equation is negative one times (2.10) is helpful, because the next stage will subtract this value from the ideal current. When choosing values for the passive components, they should be chosen according to the poles zeros and gain, which is discussed in detail in chapter 4.

3.4.2 Current Sensing and PI Controller

After the circuit generates the ideal current, this is subtracted from the actual current. This requires sensing of the average current into the amplifier, which is done using resistor and a constant gain amplifier. The error signal is fed through a proportional-integrating (PI) controller, which forces the actual current to be very close to the ideal current PI controller have gains in the form of $\frac{K_i}{s} + K_p$ where K_i is the integrating gain and K_p is the proportional gain. Additionally, the converter must determine if the DC-DC converter should source or sink current. The output of this is proportional to the duty cycle given to the converter.

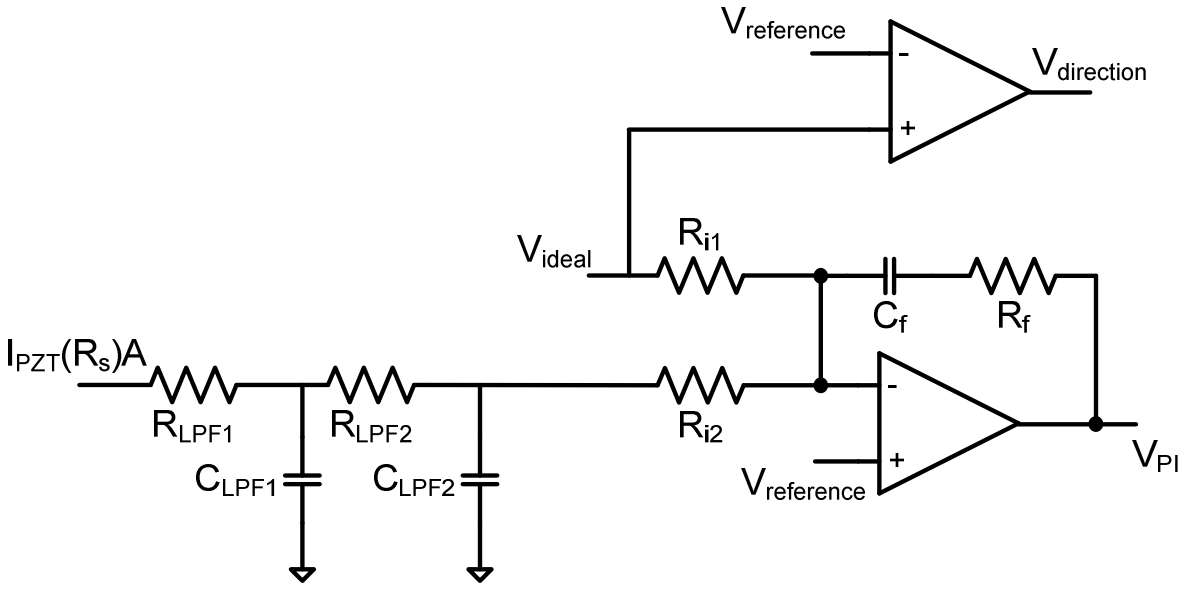

Figure 3.5 Schematic of current sensing and PI controller

Figure 3.5 shows the circuit schematic for current sensing and the PI controller. The ideal current is compared to the reference voltage (representing an ideal current of zero) in order to determine which mode the DC-DC converter should operate in as represented by the digital bit $V_{direction}$.

The actual current is sensed using a resistor and a constant gain amplifier with gain A. To obtain the average current, the sensed current is placed through a 2-pole low pass filter. The filter should have a gain of ~1 at the PZT excitation frequency, but very large attenuation at the switching frequency. The filter values must be chosen, so that the impedance of the filter is much lower than the impedance of the next stage. If this is not possible with reasonable values, it may be necessary to employ an active filter as the second stage.

$$V_{PI} = \left(\frac{1}{sC_f} + R_f\right)\left(\frac{I_{PZT}R_sA}{\left(\frac{s}{\omega_{p1}}+1\right)\left(\frac{s}{\omega_{p2}}+1\right)R_{i2}} - \frac{V_{ideal}}{R_{i1}}\right) \tag{3.17}$$

The output voltage of this stage is given by (3.17), given I_{PZT} is the PZT current, V_{ideal} is the voltage representing the ideal current, and the low pass filter for the current sense has poles ω_{p1} and ω_{p2}. Under the assumption ω_{p1} and ω_{p2} are not relevant at the PZT excitations, this equation is a weighted difference (allowing for additional gain of the either stage) of the sensed current, and ideal current, multiplied by a definable PI controller. The PI controller should be defined so that the gain at the excitation frequency is very high, but may affect stability if the PI controller is too fast (or the pole is at too high of a frequency).

3.4.3 PWM generator

The output of the PI controller provides a voltage that is proportional to the intended duty cycle for the converter. There is also a digital signal that indicates if the controller should be in buck mood or boost mode. The information from the digital signal and the PI controller must be combined by the PWM generator to create and send a PWM signal to the correct gate, with the correct duty cycle.

To generate a PWM signal from a voltage a voltage ramp and a comparator is the easiest generation method. There are a number of timers and comparators that can be chosen to do this based on switching frequency, power consumption and acceptable errors. For the purposes of these simulations, an ideal ramp and comparator is used. Real testing will require the selection and use of real components.

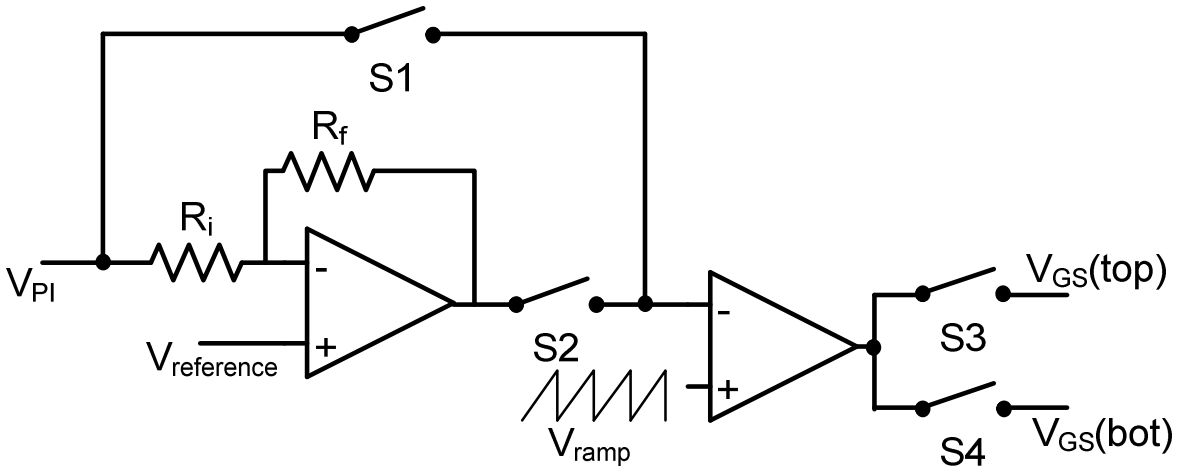

Figure 3.6 Proposed PWM generation system

The full scheme for the PWM generation system can be seen in Figure 3.6. When the system is in buck mode transferring power from the PZT to the battery, the duty cycle should be increased if the observed current is too high, and decreased if the observed current is too low. Conversely, if the system is in boost mode transferring power from the batter to the PZT, duty cycle should be decreased if the observed current is too high, and decreased if the observed current is too low (the current sense does absolute current, not the magnitude of the current). For this reason it is necessary to invert the signal controlling boost mode.

The inversion of the signal is done with an op amp. The inclusion of an op-amp, as shown not only inverts the signal but also allows for independent tuning of the loop gain for

buck-mode and boost-mode. As discussed earlier, and seen in (3.11) and (3.14), the gain il/d is different for both modes, which needs to be accounted for in the PI controller and loop gain generation.

The choice of which switch to excite is digitally chosen by a comparator, which compares the ideal current to zero current as discussed previously. If the ideal current is into the DC-DC converter, then S1 and S3 are closed, while S2 and S4 are open. The ramp comparator then uses the non-inverted output of the PI controller, and operates the top switch of the bi-directional DC-DC converter. If the ideal current is out of the DC-DC converter, then S1 and S3 are open, while S2 and S4 are closed. The ramp comparator then uses the inverted output of the PI controller, and operates the bottom switch of the Bi-Directional DC-DC converter.

$$\frac{d}{V_{PI}} = \frac{1}{V_{ramp}} \tag{3.18}$$

$$\frac{d}{V_{PI}} = -(\frac{R_f}{R_i})\frac{1}{V_{ramp}} \tag{3.19}$$

The relationship between the input and the output can be given by (3.18) for buck mode and (3.19) for boost mode, where V_{in} is the output from the PI controller, and V_{ramp} is the peak to peak voltage of the voltage ramp. As discussed, this allows for independent turning of both loop gains.

4: Small Signal Analysis

This section will provide a small signal analysis of the proposed system. The full analytical expression for the loop gain will be derived, along with the analytical expression for the input impedance. Using the loop gain and input impedance, an analysis of stability, and

expected power transfer will be done. Combining these analyses, the poles and zeroes for the input impedance will be chosen, along with the values for the PI controller. Finally, the expected power transfer will be calculated, taking into account all linear effects.

4.1 Derivation of Loop Gain and Input Impedance

Below is a small signal analysis for the loop gain and input impedance. The loop gain is based on parameters derived from section 3.

4.1.1 Loop Gain and Stability

Using the information compiled in section 3, it is possible to calculate the loop gain of the full system.

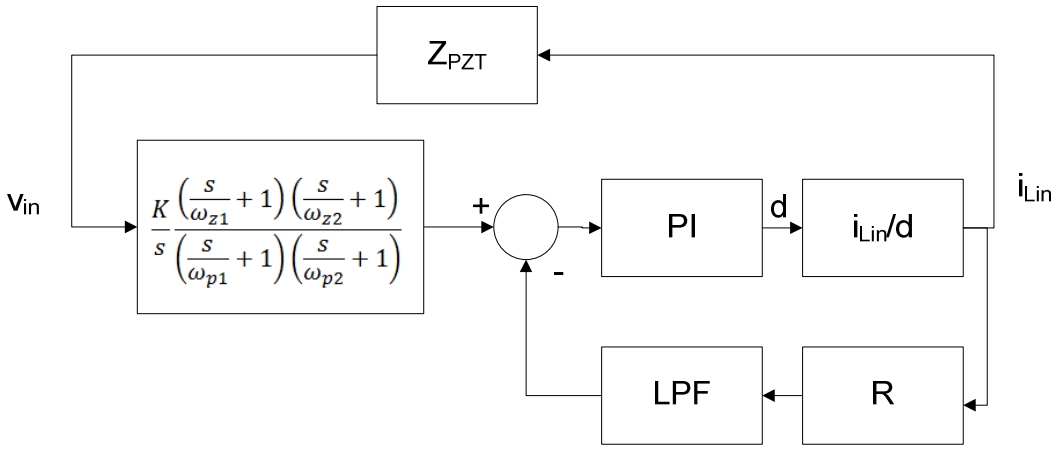

Figure 4.1 Block diagram of full system.

The block diagram of the full system can be seen in Figure 4.1. The target input impedance is the block on the far left, given by the system of poles and zeroes in (2.10). When the circuit is operating in its desired operating range, this is the actual input impedance. The difference operator is implemented by an op-amp, as discussed in section 3. The four blocks making up the feedback loop are on the bottom right. This control loop is responsible for

keeping the error between the actual current and the input current as low as possible, and should have a high gain at the relevant PZT excitation frequencies.

The PI block represents the PI controller, multiplied by the PWM generator gain. The equation for the PI controller can be given by $\frac{K_i}{s} + K_p$, as discussed earlier, while the PWM gain can be given by (3.18) for buck mode and (3.19) for boost mode. The PI block is the easiest to change, and the critical design block for tuning the feedback loop.

The block $\frac{\hat{\imath}_{PZT}}{\hat{d}}$ represents the small signal change in current as a result of a small signal change in duty cycle. For buck mode, $\frac{\hat{\imath}_{PZT}}{\hat{d}}$ can be given by (3.11), while for boost mode it is given by (3.14). As can be seen both equations are different, and are a function of V_{PZT} and D, both of which will change over operation. Because the switching frequency is much faster than the PZT excitation frequency it is possible to model this as a large range of DC operating points, but still causes complications as there is a parameter in the loop gain which changes during operation. The difference in gain between the two systems can be alleviated through proper design of the PWM gain (3.18) and (3.19), which may be defined in by the user. After that, the PI controller must be tuned to work with a large range of values for $\frac{\hat{\imath}_{PZT}}{\hat{d}}$.

The R parameter represents the gain between the input current, and the sensed voltage representing it, which is given by the current sense resistor times the gain of the current sense amplifier. The LPF parameter is the low pass filter to get the "average" current after switching ripple has been filtered out. This filter should not have a large effect on the loop gain.

$$T = \frac{\frac{K}{s}\frac{\left(\frac{s}{\omega_{z1}}+1\right)\left(\frac{s}{\omega_{z2}}+1\right)}{\left(\frac{s}{\omega_{p1}}+1\right)\left(\frac{s}{\omega_{p2}}+1\right)}\left((PI)\left(\frac{\hat{\imath}_{PZT}}{\hat{d}}\right)\right)}{(PI)\left(\frac{\hat{\imath}_{PZT}}{\hat{d}}\right)(R)(LPF)+1} Z_{PZT} \tag{4.1}$$

$$T \approx \frac{\frac{K}{s}\frac{\left(\frac{s}{\omega_{z1}}+1\right)\left(\frac{s}{\omega_{z2}}+1\right)}{\left(\frac{s}{\omega_{p1}}+1\right)\left(\frac{s}{\omega_{p2}}+1\right)}}{(R)LPF} Z_{PZT} \tag{4.2}$$

Combining terms and solving, the loop gain T can be given by (4.1). For the entire system to be stable, the loop gain must be stable, with acceptable gain and phase margins. If the PI controller is properly designed, (4.2) can be used as a reasonable estimate of the loop gain. This assumes that $(PI)\left(\frac{\hat{\imath}_{PZT}}{\hat{d}}\right)(R)(LPF) \gg 1$. The loop gain is the primary restriction on which input impedances may be defined, and determines if and when use of unstable poles and zeroes will cause the entire system to be unstable.

4.1.2 Derivation of Input Impedance

The input impedance may be derived using the block diagram shown in Figure 4.1. To derive the input impedance, a "test" signal is applied to the input voltage, and the input current is observed.

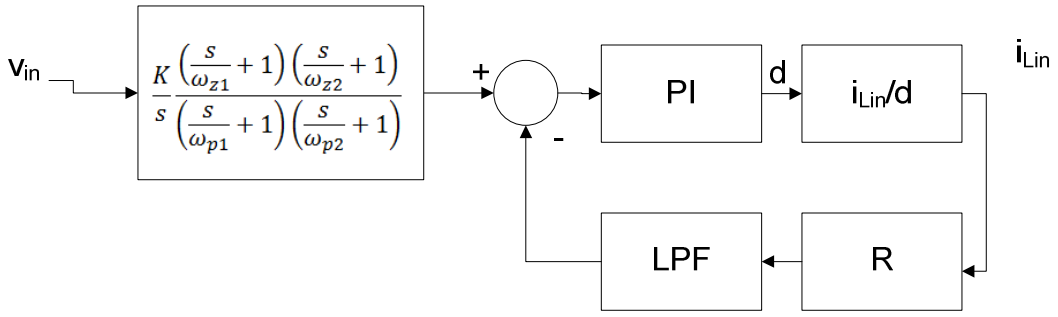

Figure 4.2 Input impedance of the system.

Figure 4.2 shows the block diagram that is to be used to determine the input impedance of the full system. Examining the effect of V_{in} on i_{Lin} removes the effect of the PZT impedance. This makes sense intuitively, as the input impedance of the converter should not be dependent on the output impedance of the prior stage.

$$Y_{in} = \frac{i_{Lin}}{V_{in}} = \frac{\frac{K}{s}\frac{\left(\frac{s}{\omega_{z1}}+1\right)\left(\frac{s}{\omega_{z2}}+1\right)}{\left(\frac{s}{\omega_{p1}}+1\right)\left(\frac{s}{\omega_{p2}}+1\right)}\left((PI)\left(\frac{\hat{\imath}_{PZT}}{\hat{d}}\right)\right)}{(PI)\left(\frac{\hat{\imath}_{PZT}}{\hat{d}}\right)(R)(LPF)+1} \tag{4.3}$$

$$Y_{in} = \frac{i_{Lin}}{V_{in}} \approx \frac{\frac{K}{s}\frac{\left(\frac{s}{\omega_{z1}}+1\right)\left(\frac{s}{\omega_{z2}}+1\right)}{\left(\frac{s}{\omega_{p1}}+1\right)\left(\frac{s}{\omega_{p2}}+1\right)}}{(R)} \tag{4.4}$$

Solving for the input admittance of the system yields (4.3). If the PI controller and the low pass filter are properly designed, (4.4) can be used as a reasonable estimate of the loop gain. This assumes that $(PI)\left(\frac{\hat{\imath}_{PZT}}{\hat{d}}\right)(R)(LPF) \gg 1$, and at relevant frequencies to the input impedance, the low pass filter is approximately one.

As can be seen, (4.4) is in the same form as the target impedance originally defined by (2.10). The only difference is that the entire equation is divided by the current sense gain R. To get the same gain as (2.10), simply multiply the term K by the current sense gain R, and the input impedance will be the same as the designed input impedance.

4.2 Choice of Circuit Parameters

Combining all of the previous equations, it is now possible to choose the parameters for the circuit, and define the input impedance. The input impedance should be designed for maximum power transfer at the frequency range around resonance. The process and selection of parameters are discussed in this section.

4.2.1 Design Process

Recall from earlier that the ideal input impedance is the complex conjugate of the output impedance of the PZT. The goal of the design is to shape the input impedance of the equation defined by (4.3) to the complex conjugate Figure 2.6. From a trending perspective, this means that the phase needs to have a positive 90 degree phase shift (provided by the low frequency zero), with a resonant peak near 16 Hz (which is provided by the poles, then the zeroes). Ideally, the magnitude should have the same magnitude near resonance (which can be done easily by changing the value of k) while trending downwards.

Because the resonant peak of the phase, as well as the ripple to the magnitude is symmetrical around resonance, it was theorized that the ideal selection of poles and zeroes for the given design assumed that the poles and zeroes would be mirrored around the resonant frequency, with K chosen to place the magnitude at the right value (as it doesn't affect the phase). A brute force solver was implemented with these parameters, designed to maximize the integral

of the power transfer, which should corresponding to the most energy harvested from a noisy or unpredictable vibration energy source. The values chosen are: K/R= 365, ω_{z1}=85, ω_{z2}=85, ω_{p1}=115, and ω_{p2}=115.

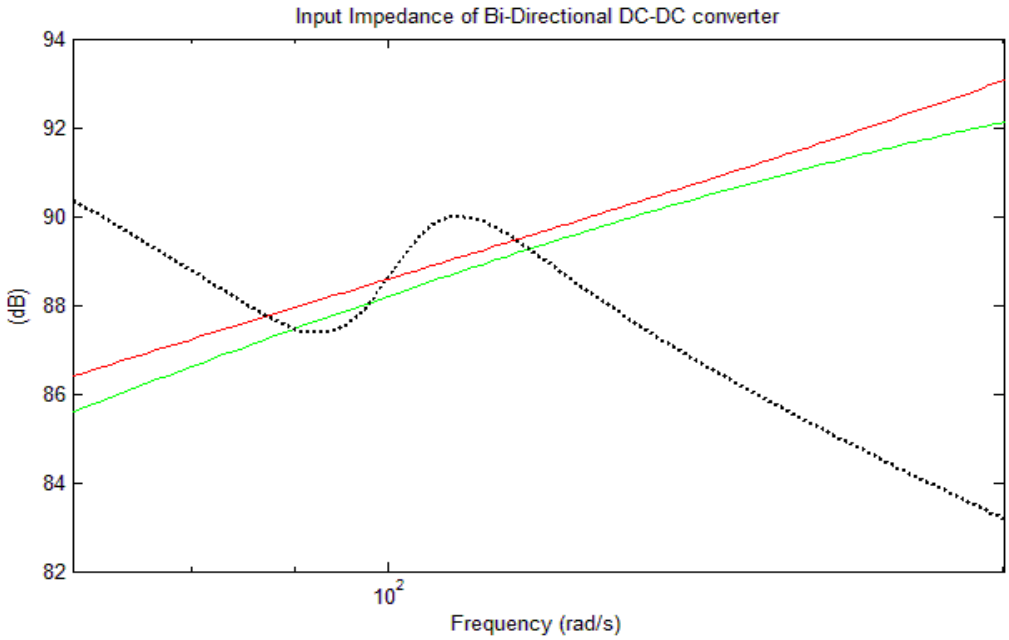

Figure 4.3 Magnitude of the complex conjugate of the designed input impedance (red) the input impedance of an RL match (green) and the target input impedance (black)

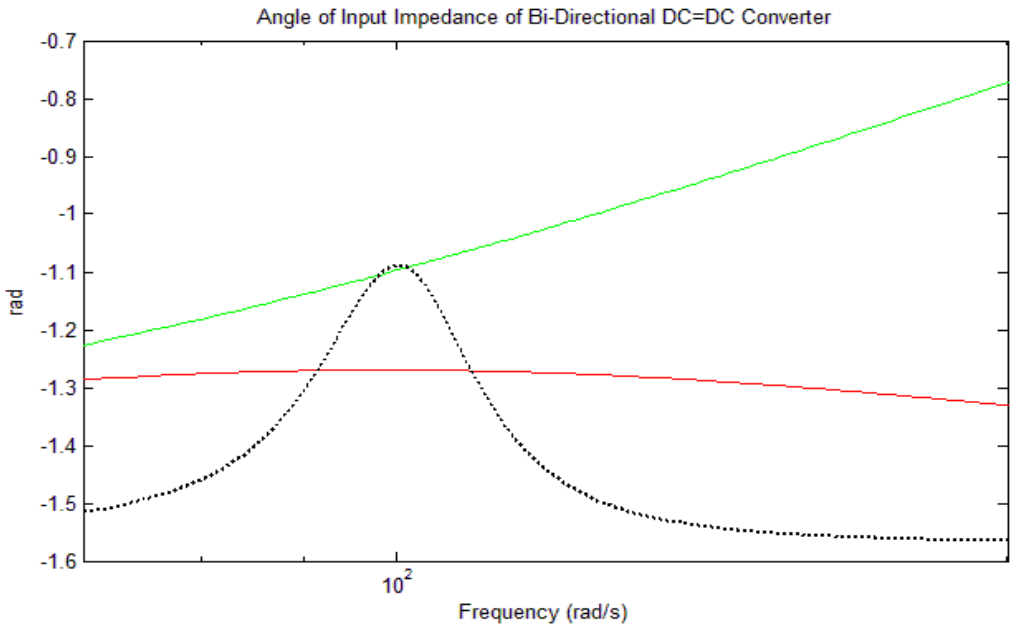

Figure 4.4 Phase of the complex conjugate of the designed input impedance (red) the input impedance of an RL match (green) and the target input impedance (black)

Figure 4.3 and Figure 4.4 show the phase and magnitude output impedance of the PZT, along with the complex conjugate of a traditional RL match, as well as the complex conjugate of the input impedance of the proposed DC-DC converter. The complex conjugates are shown instead of the actual value, for easy viewing, as the dotted black line is now the "ideal" impedance, to which we are trying to match.

As can be seen in Figure 4.4, the curvature of the phase is closer to the ideal curvature for the DC-DC converter than the traditional RL match, allowing for a broader band match. The magnitude shown in Figure 4.3 shows a comparable match. Because the proposed system has an input impedance close to the ideal input impedance over a larger frequency range than the RL match, the bandwidth of the proposed match will be higher than that of the traditional RL match.

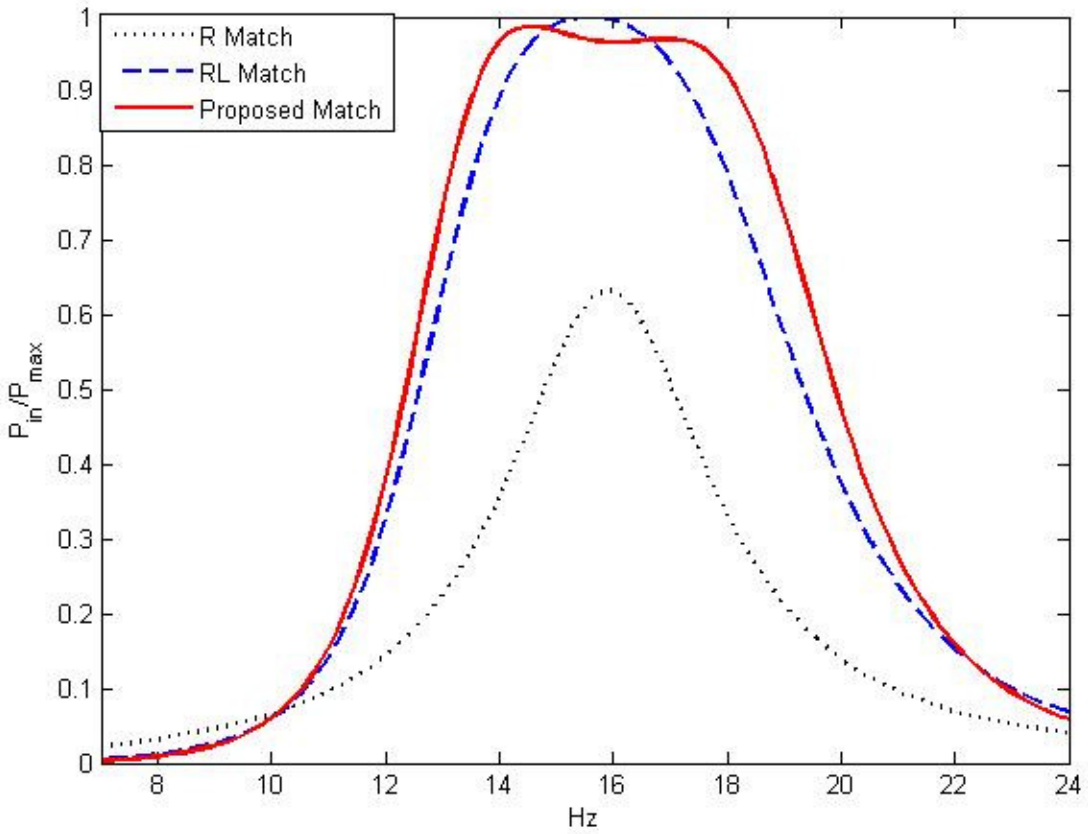

Figure 4.5 Expected power transfer for R match, RL match, and proposed match

Recalling the power transfer equation discussed earlier, and presented in (2.7), along with the chosen parameters plugged into (4.3), and the PZT impedance defined earlier by it is possible to determine the power transfer at any frequency. This was done in MATLAB, with the available power normalized to be 1mW at each excitation frequency, through changing the value of the I_{AC} in the current source model. Figure 4.5 shows the power transfer of this system, compared to the power transfer of an ideal RL match, and an ideal R match. As expected the R match is far inferior to both reactive matching techniques, as the advantages of the R match lie in simplicity, not power consumption. The proposed match shows an incremental improvement over the traditional RL match, all of which is "gained" energy, because they have the same complexity of implementation.

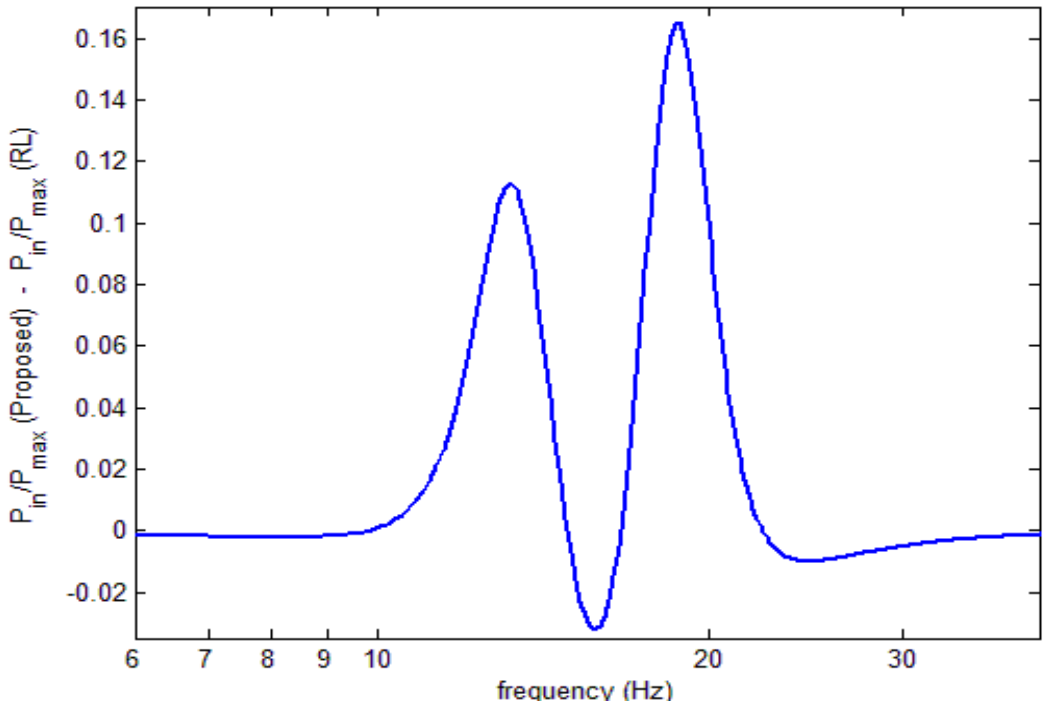

Figure 4.6 Difference in power transfer for RL match and proposed match

Figure 4.6 shows the difference between the RL match, and the proposed match. The proposed match is superior to the RL match at most frequencies, extracting up to 16% more of the available energy at the frequencies around resonance. This corresponds to 160uW extra given our 1mW excitation. At resonance, where the RL match was designed to optimize, the RL match has a slight edge on the actual match, delivering a maximum of 4% more of the total available energy, corresponding to a loss of 40uW at exactly resonance given our 1mW excitation.

The analysis done in this section proves that the control system is stable, and that under the correct assumptions the input impedance is reasonably close to the target impedance defined by (2.10). It also shows that the input impedance can be designed to give better broadband power transfer than the traditional RL match. Because the only published methods of RL

matching a PZT cantilever have the same implementation procedure as our match, this energy is gained without notable increases to the complexity of the control circuitry. This design process does, however require prior knowledge of the model for the target PZT cantilever.

5: Results

To confirm the analytical results, simulations of the proposed topology were run, and compared to the analytical results. The simulation and results are explored in this section, and expected control losses are estimated

5.1 Simulation Methodology

Simulations were run in SIMETRIX by SIMPLIS technologies. The current source model seen in Figure 2.4 was used to simulate the PZT source, at a single given frequency. Simulations were normalized so that the perfectly matched PZT would have 1mW of power available at any frequency. This normalization corresponds to a constant base acceleration of the PZT cantilever, at different frequencies.

A fully analog implementation, as seen in section 3 was used in the simulation. Ideal op-amps were used in the implementation, as well as ideal comparators. After determining the pole/zero values, which are discussed in section 4, the other parameters and RC values may be trivially determined, and are not discussed in detail (although were chosen for the implementation). An ideal amplifier was also used for detection of the current into the DC-DC converter.

Because some of the energy must enter and leave the converter multiple times, switching losses are difficult to calculate analytically. To come up with an idea of efficiency, and loss due

to conduction, a switch with on channel resistance of 1.2 Ω, and the SIMETRIX typical Schottky diode, this diode has a forward drop of about 0.3 V. These values were chosen to be reasonable for discrete parts on a low power system.

As discussed, the energy will resonate in and out of the DC-DC converter, making it hard to determine the instantaneous power in. In order to determine the average power harvested, long transient simulations were run, and the average current into the battery was examined in steady state. To get a better average, the averaging window for the current was a whole number multiple of the period of the PZT excitation frequency. This ensures that there is not any "half" PZT periods averaged where current may be flowing only into or out of the converter.

5.2 Simulation Results

Transient simulation results were analyzed, and the average battery currents were compared to the expected battery current. Results are presented here.

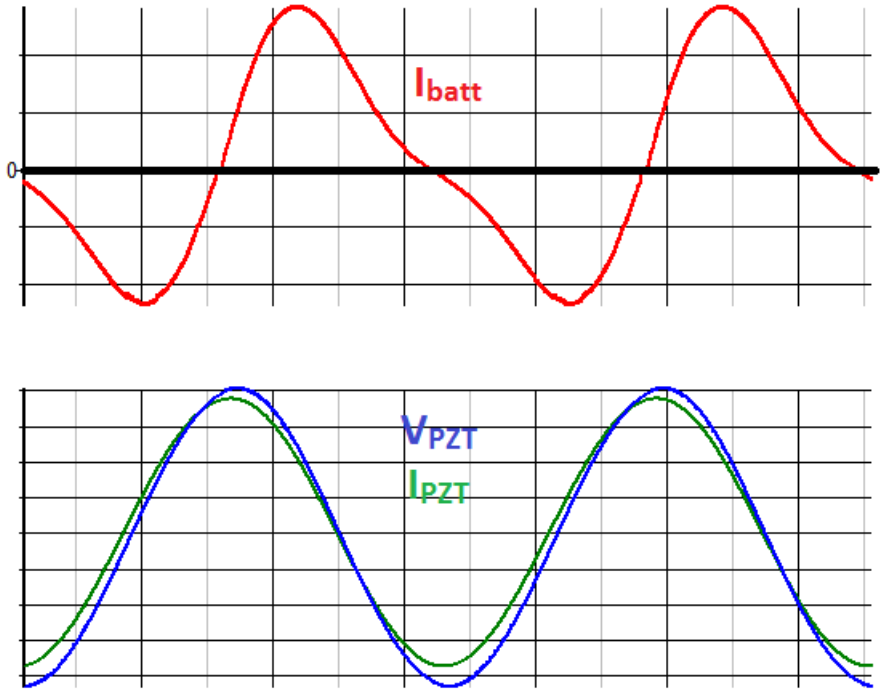

Figure 5.1 Switching waveforms near resonance.

Figure 5.1 shows a transient result for operation at the resonant frequency of 15.9 Hz. The top graph shows the average current flowing into the battery and the bottom graph shows the input voltage and PZT excitation current. The excitation current and input voltage are well in phase with each other, indicating a good complex conjugate match. The amount of current which the battery sinks for high input voltage is larger than the amount it sources for low input voltage, yielding overall positive power transfer.

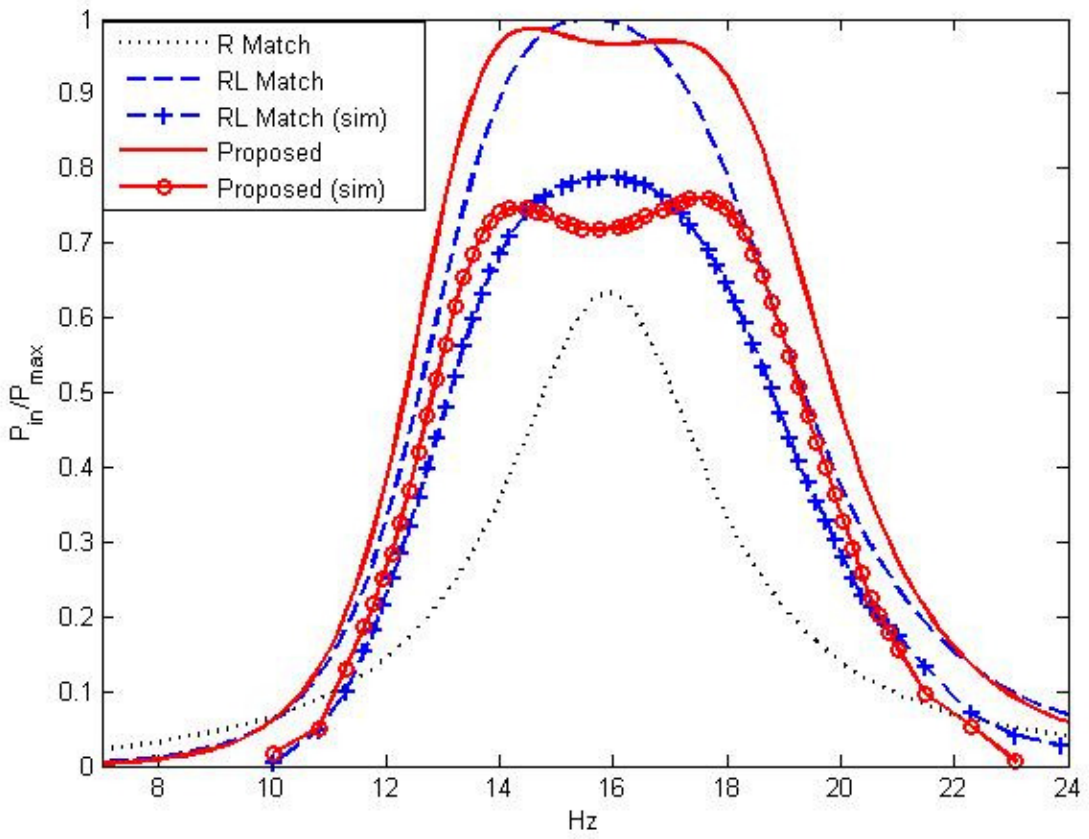

Figure 5.2 Full system efficiency for three systems, with simulations for both reactive matches

Figure 5.2 shows analytical results with ideal components for the efficiency of the three different methods, an RL match, a resistive match, and the proposed system. As expected, both the RL match and the proposed one achieve far higher efficiency than the resistive matching. The proposed system has two peaks to widen the bandwidth, while the RL match has only one peak at resonance. The bandwidth of the proposed system for over 90% efficiency is 4.60 Hz, while that for the RL system is 3.35 Hz. So, the proposed system increases the bandwidth by 37% when compared with the RL match.

The RL match and the proposed system were implemented with analog components and simulated with practical components with losses as described in the earlier, and discrete points

are marked by "+" and "o." The efficiency of both systems is reduced to about 75% for the frequency range simulated. So the bandwidth of the proposed system at the 90% of the peak power of the RL system is wider by 37% compared with the RL system.

5.3 Comparison to Analytical Results

If implementation of this system is to be practical, analytical input resistance discussed in (4.3) must be reasonably close to the actual input impedance, or the system will not resonate. Since the harvestable power is directly related to the input impedance, a comparison of the expected power outputs is the simplest and most effective method of doing so.

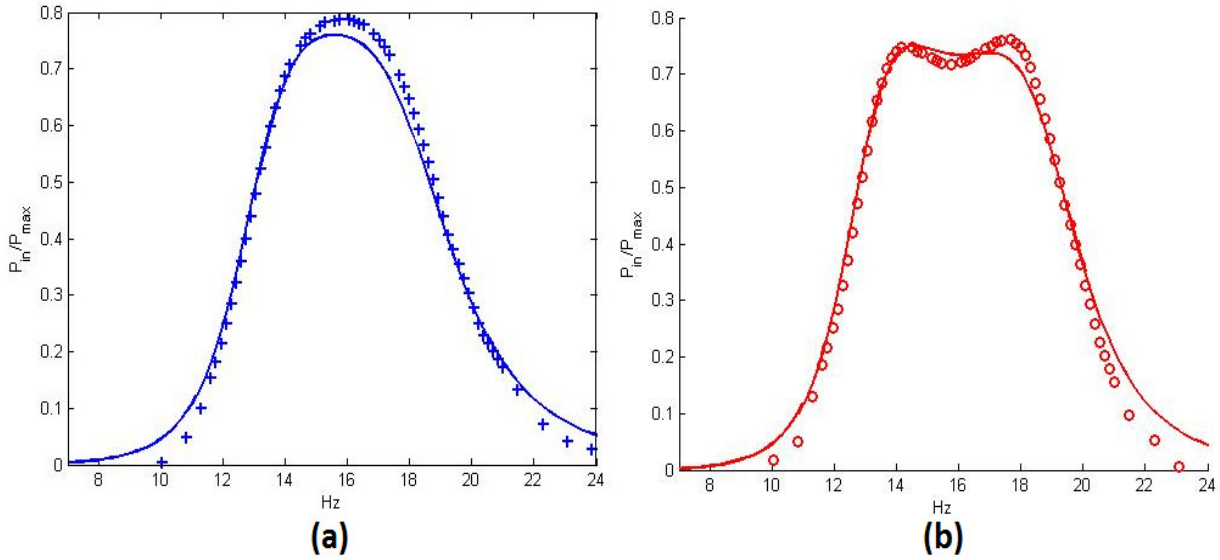

Figure 5.3 Comparison of expected results and simulated results for (a) RL match and (b) proposed match

A comparison of results can be seen in Figure 5.3, for both the R and RL match. The individual points represent the simulated points, while the line shows the theoretical results multiplied by 0.76, corresponding to an expected 76% efficiency. In both graphs, the expected results for this topology are reasonably close to the simulated results, validating the analytical

model. In both graphs, the results show slightly higher efficiency when there is a lot of power available, and poor efficiency when there is not much power available (dropping off sharply near 0.15 mW of available power). This result is not surprising, as the benefit of transferring energy to the battery and back many times will not be very large when there is not much power expected in the first place.

The two largest sources of error are varying efficiency, and varying of the parameter $\frac{\hat{\imath}_{PZT}}{\hat{d}}$ during operation. The efficiency is very hard to model because it is a function of PZT voltage, frequency, and switching mode, all of which change while operating. Further, some energy must go into the converter and back out of the converter before being stored in the battery, which further convolutes efficiency calculations. This is why the simulations were used to estimate efficiency, and the 76% quoted efficiency is only an estimate of the typical overall efficiency including all of these effects.

Changing of parameter $\frac{\hat{\imath}_{PZT}}{\hat{d}}$ (which was discussed in section 3) also adds error to the model. The PI controller can be designed so that a very large range of values yields approximately the same value, but there are some conditions (right before the mode switches in specific) where $\frac{\hat{\imath}_{PZT}}{\hat{d}}$ becomes very low and can cause slight error.

Despite these sources of error, the analytical model is reasonably close to the observed results, and may be used to design a well matched system.

5.4 Estimation of Control Losses

As the target system is very low power, the control losses will be significant and proper low power design of the control loop will be critical. The following is an example design,

showing what sort of losses can be expected due to control, assuming three series nickel-metal hydride (NiMH) batteries with a 3.6 V nominal operating voltage.

Four Operational Amplifiers are used in the control loop. Because their performance will affect the loo gain, gain bandwidth must be reasonably high, above approximately 500kHz, eliminating true low power op-amps such as the AD8659. A good choice for the operational amplifiers is the AD4096-4, a quad op-am with 60µA supply current per channel with 800KHz gain bandwidth.

Ramp Generation can be done using a comparator connected similarly to that presented by Kong et al. [24]. An additional comparator will be used to generate a PWM from the generated ramp, and a third comparator will be used to sense the polarity of the input voltage. The ADCMP371 is a simple comparator capable of this, and consumes 4 uA of current.

Current sense amplification must be done with an instrumentation amplifier, preferably a variable gain instrumentation amplifier so to allow for flexibility in the other feedback loops. The INA333 has a current consumption of 50 uA, and a variable gain between 1 and 100 V/V.

PZT voltage sensing must occur with a resistive divider, which must be high enough impedance to be low power, but low enough impedance to allow accurate sensing. 1 MΩ is a fair estimation of an accurate voltage sense divider.

Table 5.1. Expected power consumption of control circuitry

Device Description	Part #	Supply Current (uA)	Power (uW)
Input Buffer Op Amp	ADA4096-4	60	216
Target Current Generator Op Amp	ADA4096-4	60	216
PI Controller Op Am	ADA4096-4	60	216
Duty Cycle Inversion Op-Amp	ADA4096-4	60	216
Input Polarity Comparator	ADCMP371	4	14.4
Ramp Comparator	ADCMP371	4	14.4
Instrumentation Amplifier	INA333	50	180
Ramp Generator	ADCMP371	4	14.4
1 MΩ Voltage Divider at 10V RMS		N/A	100
TOTAL		302	1187.2

Table 5.11 shows the current consumption of each individual component, and the power consumption assuming the 3.6 V nominal voltage of the battery. The total control circuitry consumes 1.187 mW of power using these assumptions.

Using this, it is possible to estimate how much energy must be available from the example PZT, for this technique to be viable, when compared to the energy harvested from the ideal resistive match. The integral of harvestable power from the proposed match in Figure 5.2 is 2.24 times larger than that of the resistive match. Assuming that the proposed match operates at 75% efficiency (as suggested by simulation results) and that the resistive match operates at 100% efficiency (which is unlikely, considering it to will have conduction losses and simple control circuitry), the power harvested by the proposed converter is 1.68 times greater than the resistive match.

To account for the 1.187 mW of power consumed, the available energy must be greater than approximately 2.9 mW. For systems with less than 2.9 mW of power available, this

technique is not feasible, but will begin to harvest more power as the available power increases beyond 2.9 mW.

6: Conclusion

This thesis proposed a system to widen the bandwidth of piezoelectric cantilever based energy harvesters for vibration energy harvesting, which extends the range of frequencies where near maximum power may be harvested from the cantilever. The topology proposed was based on a previously proposed method of RL matching. A novel input impedance is proposed, which was shown to provide a more broadband match, when compared to a typical RL match.

A full analysis of the proposed system was performed of the full system, as well as each individual block. Small signal analysis was performed to provide transfer functions for each individual block, and blocks were combined to predict the expected input impedance and harvested power of the full system. Transient simulations of the full system were performed at various frequencies, and the average harvested power as compared to the expected harvested power. Waveforms of the transient simulations showed in phase voltages and currents, suggesting a good complex conjugate match. Analysis of extracted power over wide range of frequencies shows that the experimental model provides reasonably good predictions for the input impedance.

For the example PZT, when compared to the existing RL match, it can be shown that the proposed method increases the frequencies which can theoretically harvest 90% of the power or more from the PZT cantilever by 37%. Due to the noisy nature of vibration energy, the ability resonate at an increased number of frequencies will be advantageous, allowing for the harvesting

of more energy from real vibration sources. While the input impedance initially looks more complex than a RL match, the required power is approximately the same, as the input impedance may be implemented with a single op-amp.

Power consumption of control circuitry was not modeled. Due to the low-power nature of most PZT cantilever sources, low power design of the control circuitry will be a critical design consideration when implementing this topology. Because the full system uses a fully analog implementation (compared to the digital control on previous systems) a very low power implementation, such as on an Integrated Circuit (IC) is feasible for this design.

Future work can include implementation of this design, and exploring alternative input impedances. Implementation could be done using low power analog components or an IC, and experimental results could be seen with real vibration sources, and real PZT cantilevers. Additionally, it may be possible to define more complex input impedances which can be used to further extend the bandwidth at the cost of complexity. This allows future work to use the analysis for the rest of the converter to predict the actual input impedance, power transfer, and loop gain of new user defined input impedances.

References

[1] M. K. Stojcev, M. R. Kosanovic, and L. R. Golubovic, "Power management and energy harvesting techniques for wireless sensor nodes," in *TELSIKS '09. 9th International Conference on Telecommunication in Modern Satellite, Cable, and Broadcasting Services, 2009.*, 2009, pp. 65-72.

[2] M. Tacca, P. Monti, and A. Fumagalli, "Cooperative and Reliable ARQ Protocols for Energy Harvesting Wireless Sensor Nodes," *IEEE Transactions on Wireless Communications,* vol. 6, pp. 2519-2529, 2007.

[3] P. Chulsung and P. H. Chou, "AmbiMax: Autonomous Energy Harvesting Platform for Multi-Supply Wireless Sensor Nodes," in *3rd Annual IEEE Communications Society on Sensor and Ad Hoc Communications and Networks, 2006. SECON '06. 2006* 2006, pp. 168-177.

[4] Y. Hongseok, S. Moonjoo, and K. Dongkyun, "Dynamic Duty-Cycle Scheduling Schemes for Energy-Harvesting Wireless Sensor Networks," *IEEE Communications Letters,* vol. 16, pp. 202-204, 2012.

[5] D. Niyato, E. Hossain, M. M. Rashid, and V. K. Bhargava, "Wireless sensor networks with energy harvesting technologies: a game-theoretic approach to optimal energy management," *IEEE Wireless Communications,* vol. 14, pp. 90-96, 2007.

[6] E. O. Torres and G. A. Rincon-Mora, "Electrostatic Energy-Harvesting and Battery-Charging CMOS System Prototype," *IEEE Transactions on Circuits and Systems I: Regular Papers,* vol. 56, pp. 1938-1948, 2009.

[7] A. Khaligh, Z. Peng, and Z. Cong, "Kinetic Energy Harvesting Using Piezoelectric and Electromagnetic Technologies - State of the Art," *IEEE Transactions on Industrial Electronics,* vol. 57, pp. 850-860, 2010.

[8] Q. Zhang, J. Zhao, K. Uchino, and J. Zheng, "Change of the weak-field properties of Pb (ZrTi) O3 piezoceramics with compressive uniaxial stresses and its links to the effect of dopants on the stability of the polarizations in the materials," *Journal of materials research,* vol. 12, pp. 226-234, 1997.

[9] A. Badel, A. Benayad, E. Lefeuvre, L. Lebrun, C. Richard, and D. Guyomar, "Single crystals and nonlinear process for outstanding vibration-powered electrical generators," *IEEE Trans Ultrasonic Ferroelectric Frequency Control,* vol. 53, pp. 673-84, Apr 2006.

[10] C. B. Williams and R. B. Yates, "Analysis of a micro-electric generator for microsystems," *Sensors and Actuators A: Physical,* vol. 52, pp. 8-11, 3 1996.

[11] A. Erturk and D. J. Inman, "A Distributed Parameter Electromechanical Model for Cantilevered Piezoelectric Energy Harvesters," *Journal of Vibration and Acoustics,* vol. 130, p. 041002, 2008.

[12] S. P. Beeby, M. J. Tudor, and N. M. White, "Energy harvesting vibration sources for microsystems applications," *Measurement Science and Technology,* vol. 17, p. R175, 2006.

[13] N. G. Elvin and A. A. Elvin, "A General Equivalent Circuit Model for Piezoelectric Generators," *Journal of Intelligent Material Systems and Structures,* vol. 20, pp. 3-9, January 1, 2009 2009.

[14] S. Roundy, E. S. Leland, J. Baker, E. Carleton, E. Reilly, E. Lai*, et al.*, "Improving power output for vibration-based energy scavengers," *IEEE Pervasive Computing,* vol. 4, pp. 28-36, 2005.

[15] Y. C. Shu and I. C. Lien, "Efficiency of energy conversion for a piezoelectric power harvesting system," *Journal of Micromechanics and Microengineering,* vol. 16, p. 2429, 2006.

[16] S. Saggini, S. Giro, F. Ongaro, and P. Mattavelli, "Implementation of reactive and resistive load matching for optimal energy harvesting from piezoelectric generators," in *2010 IEEE 12th Workshop on Control and Modeling for Power Electronics (COMPEL)*, 2010, pp. 1-6.

[17] G. Lombaert, G. Degrande, J. Kogut, and S. François, "The experimental validation of a numerical model for the prediction of railway induced vibrations," *Journal of Sound and Vibration,* vol. 297, pp. 512-535, 11/6/ 2006.
[18] G. Lombaert, G. Degrande, and D. Clouteau, "Numerical modelling of free field traffic-induced vibrations," *Soil Dynamics and Earthquake Engineering,* vol. 19, pp. 473-488, 10// 2000.
[19] T. von Buren, P. D. Mitcheson, T. C. Green, E. M. Yeatman, A. S. Holmes, and G. Troster, "Optimization of inertial micropower Generators for human walking motion," *IEEE Sensors Journal,* vol. 6, pp. 28-38, 2006.
[20] M. Ferrari, V. Ferrari, M. Guizzetti, D. Marioli, and A. Taroni, "Piezoelectric multifrequency energy converter for power harvesting in autonomous microsystems," *Sensors and Actuators A: Physical,* vol. 142, pp. 329-335, 3/10/ 2008.
[21] S. Roundy, P. K. Wright, and J. Rabaey, "A study of low level vibrations as a power source for wireless sensor nodes," *Computer Communications,* vol. 26, pp. 1131-1144, 7/1/ 2003.
[22] E. Lefeuvre, D. Audigier, C. Richard, and D. Guyomar, "Buck-Boost Converter for Sensorless Power Optimization of Piezoelectric Energy Harvester," *IEEE Transactions on Power Electronics,* vol. 22, pp. 2018-2025, 2007.
[23] N. Kong and D. S. Ha, "Low-Power Design of a Self-powered Piezoelectric Energy Harvesting System With Maximum Power Point Tracking," *IEEE Transactions on Power Electronics,* vol. 27, pp. 2298-2308, 2012.
[24] N. Kong, D. S. Ha, A. Erturk, and D. J. Inman, "Resistive Impedance Matching Circuit for Piezoelectric Energy Harvesting," *Journal of Intelligent Material Systems and Structures,* vol. 21, pp. 1293-1302, September 1, 2010 2010.
[25] G. K. Ottman, H. F. Hofmann, A. C. Bhatt, and G. A. Lesieutre, "Adaptive piezoelectric energy harvesting circuit for wireless remote power supply," *IEEE Transactions on Power Electronics,* vol. 17, pp. 669-676, 2002.
[26] G. K. Ottman, H. F. Hofmann, and G. A. Lesieutre, "Optimized piezoelectric energy harvesting circuit using step-down converter in discontinuous conduction mode," *IEEE Transactions on Power Electronics,* vol. 18, pp. 696-703, 2003.
[27] N. Kong, T. Cochran, D. S. Ha, H.-C. Lin, and D. J. Inman, "A self-powered power management circuit for energy harvested by a piezoelectric cantilever," in *2010 Twenty-Fifth Annual IEEE Applied Power Electronics Conference and Exposition (APEC)*, 2010, pp. 2154-2160.
[28] X. Shengwen, K. D. T. Ngo, T. Nishida, C. Gyo-Bum, and A. Sharma, "Converter and controller for micro-power energy harvesting," in *Applied Power Electronics Conference and Exposition, 2005*, 2005, pp. 226-230 Vol. 1.
[29] S. Xu, K. D. T. Ngo, T. Nishida, G. B. Chung, and A. Sharma, "Low Frequency Pulsed Resonant Converter for Energy Harvesting," *IEEE Transactions on Power Electronics,* vol. 22, pp. 63-68, 2007.
[30] E. Lefeuvre, A. Badel, C. Richard, and D. Guyomar, "Piezoelectric Energy Harvesting Device Optimization by Synchronous Electric Charge Extraction," *Journal of Intelligent Material Systems and Structures,* vol. 16, pp. 865-876, October 1, 2005 2005.
[31] S. Mohammadi and A. Khodyari, "Damping Analyses of Structural Vibrations and Shunted Piezoelectric Transducers," *Smart Materials Research,* vol. 2012, 2012.
[32] Y. K. Ramadass and A. P. Chandrakasan, "An efficient piezoelectric energy-harvesting interface circuit using a bias-flip rectifier and shared inductor," in *IEEE International Solid-State Circuits Conference - Digest of Technical Papers, 2009*, 2009, pp. 296-297,297a.
[33] J. Liang and W.-H. Liao, "An improved self-powered switching interface for piezoelectric energy harvesting," in *International Conference on Information and Automation, 2009.*, 2009, pp. 945-950.

[34] D. Guyomar, A. Badel, E. Lefeuvre, and C. Richard, "Toward energy harvesting using active materials and conversion improvement by nonlinear processing," *IEEE Transactions on Ultrasonics, Ferroelectrics and Frequency Control,* vol. 52, pp. 584-595, 2005.